# Taconian retrograde eclogite from northwest Connecticut, USA, and its petrotectonic implications

**Article** *in* Lithos · October 2015

DOI: 10.1016/j.lithos.2015.10.011



**4 authors**, including:

Xu Chu
Rice University
**10** PUBLICATIONS **53** CITATIONS
SEE PROFILE

Jennifer Axler
Yale University
**8** PUBLICATIONS **8** CITATIONS
SEE PROFILE

Lithos 240–243 (2016) 276–294

Contents lists available at ScienceDirect

Lithos

journal homepage: www.elsevier.com/locate/lithos

Invited research article

# Taconian retrograde eclogite from northwest Connecticut, USA, and its petrotectonic implications

Xu Chu [a,*], Jay J. Ague [a,b], Jennifer A. Axler [a], Meng Tian [a]

[a] Department of Geology and Geophysics, Yale University, P.O. Box 208109, New Haven, CT 06520-8209, USA
[b] Peabody Museum of Natural History, Yale University, New Haven, CT 06511, USA

ARTICLE INFO

*Article history:*
Received 1 June 2015
Accepted 25 October 2015
Available online 30 October 2015

*Keywords:*
Eclogite
Taconic orogeny
Pseudosection
Symplectite
New England

ABSTRACT

Mafic lenses hosted by felsic paragneiss in a Taconic thrust slice (Canaan Mountain Formation) from northwest Connecticut (New England, USA) contain relict mineral assemblages and decompression textures indicative of high pressure (HP) precursors. Symplectic intergrowths consisting mostly of diopside + plagioclase or biotite + plagioclase are pseudomorphous after omphacite and phengite, respectively. Pseudosection analysis and thermobarometry demonstrate that the inferred peak assemblage of garnet + clinopyroxene + phengite formed at >14 kbar and ~710 °C in the eclogite facies. Bulk-rock geochemistry and field relations indicate that the protoliths of the mafic gneisses were likely rifting-related mafic intrusions. Zircon U–Pb dating by ion probe yields a 456 ± 4.6 Ma (2σ) metamorphic age for the mafic gneiss. The zircons from the felsic host rocks have an identical 456 ± 11 Ma metamorphic rim age and Grenvillian detrital cores. The HP metamorphism and the coeval arc magmatism reflect the collision between the Laurentian passive margin and a Taconic arc complex over an east-dipping subduction zone that was active until ~456 Ma in Connecticut (southern New England). The *P–T* path is characterized by post-peak-*T* compression, suggesting that the eclogite-facies metamorphism was associated with the deformation of the collision zone after the initial continent–arc collision. After the culmination of collision the subduction polarity switched; metamorphic ages decrease southward along the orogen suggesting that this reversal occurred ~10 Myr later in New England than in Newfoundland. Nearly all mafic rocks in the study area crop out as fairly ordinary-looking amphibolites, so it is reasonable to speculate that HP metamorphism was more extensive than currently recognized in New England but has been obscured by thermal overprinting and retrogression.



## 1. Introduction

The Taconic orogenic belt on the eastern margin of Laurentia records the collision of the Laurentian passive margin with a magmatic arc or arcs over an east-dipping subduction zone (e.g., Karabinos et al., 1998; Macdonald et al., 2014; Ratcliffe et al., 1998; Stanley and Ratcliffe, 1985; van Staal et al., 2012). The collision led to the closure of the Humber Seaway, which was followed by the closure of the Iapetus Ocean, and ultimately Paleozoic supercontinent amalgamation (Fig. 1A; e.g., Waldron et al., 2014; van Staal et al., 2012).

The orogenic belt extends thousands of kilometers from Georgia (USA), to Newfoundland (Canada), and further north to the British Isles, connecting to the Caledonian orogenic belt between Greenland and Baltica (Fig. 1A). Despite large-scale subduction and continent–arc collision, high-pressure (HP) eclogites and blueschists of Taconic age have only been described from a limited number of localities in the Appalachians, including North Carolina (Page et al., 2003; Willard and Adams, 1994), Vermont (Laird and Albee, 1981) and Newfoundland (De Wit and Strong, 1975; Jamieson, 1990) (Fig. 1A). In addition, rocks inferred to be retrograded eclogites have been reported from northwestern Connecticut (Harwood, 1975; Maggs, 1984; Maggs et al., 1986), southeastern New York (Mihok-Trenka, 2004), and Québec (Trzcienski, 1988). For these latter three occurrences, the original metamorphic conditions were masked to varying degrees by retrogression and/or regional thermal overprinting, making it difficult to verify eclogite facies pressure–temperature conditions. Thus, the rocks are currently not considered to be confirmed eclogite localities (e.g., Spray, 1988).

The rarity of HP rocks in eastern North America contrasts with the presence of HP and ultrahigh-pressure (UHP) rocks in the Greenland and Norwegian Caledonides (ca. 420–400 Ma; e.g., Carswell et al., 2003; Gilotti et al., 2004). A persistent question is whether this lack of HP rocks reflects widespread overprinting, or the uncommon attainment of blueschist–eclogite facies conditions.

Massive, meter-scale mafic gneiss lenses are embedded in highly deformed felsic paragneiss of the Canaan Mountain Formation in northwest Connecticut (Figs. 1C, 2). Regional mapping shows that the mafic gneisses probably originated as dikes or volcanic flows; relict mineralogy and symplectic textures are suggestive of high-pressure precursors (Harwood, 1975; Maggs, 1984; Maggs et al., 1986). In the

* Corresponding author. Tel.: +1 203 436 9091.
*E-mail address:* xu.chu@yale.edu (X. Chu).

http://dx.doi.org/10.1016/j.lithos.2015.10.011
0024-4937/

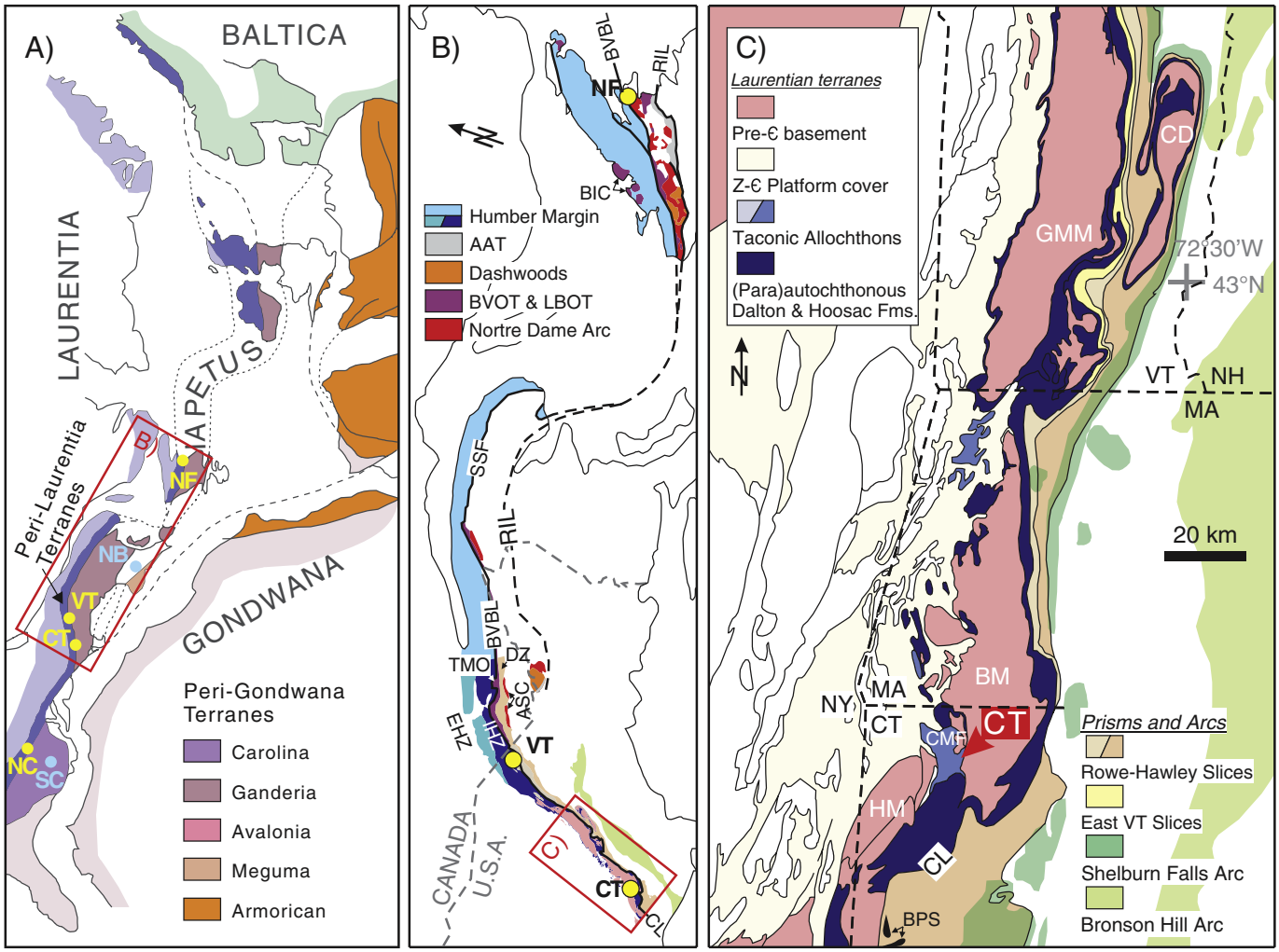


**Fig. 1.** (A) Paleogeography of Laurentia–Gondwana–Baltica and Iapetus tectonic terranes prior to the opening of the Atlantic Ocean. Localities of eclogites in the Appalachians are labeled. Yellow circles for Taconic ages: Newfoundland (NF; De Wit and Strong, 1975; Jamieson, 1990); Vermont (VT; Laird and Albee, 1981); Connecticut (CT; this study); North Carolina (NC; Page et al., 2003; Willard and Adams, 1994). Blue circles for pre-Taconic ages: New Brunswick (NB; White et al., 2001); South Carolina (SC; Dannis et al., 2000; Shervais et al., 2003). (B) Tectonic map of the Taconic orogenic belt of the Canadian and New England Appalachians. The localities of Taconic eclogites are marked. (C) Regional geology of the New England Taconic Orogen. The study area is marked. AAT: Annieopsquotch Accretionary Tract; ASC — Ascott Complex; BM — Berkshire Massif; BIC — Bay of Islands Complex; BPS — Brookfield Plutonic Series; BVBL — Baie Verte–Brompton Line; BVOT — Baie Verte Oceanic Tract; CD — Chester Dome; CL — Cameron's Line; CMF — Canaan Mountain Formation; DZ — Dunnage Zone; EHZ — External Humber Zone; GMM — Green Mountain Massif; HM — Housatonic Massif; IHZ — Internal Humber Zone; LBOT — Lushs Bight Oceanic Tract; RIL — Red Indian Line; SSF — Shickshock Sud Fault; TMO — Thetford-Mines Ophiolite.
(A) Modified after van Staal et al. (2012). (B) Modified after van Staal and Barr (2012) and Castonguay et al. (2012). (C) Modified after Stanley and Ratcliffe (1985) and Karabinos et al. (1998).

least-retrogressed rocks, spectacular symplectic pseudomorphs consist of: 1) diopside + plagioclase + orthopyroxene + quartz + oxides or 2) biotite + plagioclase + oxides. The diopside + plagioclase symplectite is widely interpreted to be pseudomorphous after Na-rich clinopyroxene (e.g., Anderson and Moecher, 2007; Eskola, 1921; Franceschelli et al., 2007; Nakano et al., 2010; Vogel, 1966; Will and Schmädicke, 2001). Some symplectic diopside is further hydrated to hornblende and actinolite. The biotite + plagioclase intergrowth is interpreted as the breakdown product of phengite or phengite + omphacite (e.g., Franz et al., 1986; Janak et al., 2012). Both textures are common decompression features in HP or UHP eclogites. Nevertheless, whether the mafic gneisses were HP mafic granulites or actually reached eclogite facies conditions remains highly uncertain because of strong amphibolite facies retrogression.

Controversy persists regarding the timing of Taconic metamorphism, particularly in southern New England. The Taconic orogenic belt was intensely overprinted by the following Salinic (~425 Ma) and Acadian (~400 Ma) thermal events; thus, $^{39}Ar/^{40}Ar$ dating generally yields younger ages than the Taconian deformation and magmatism (Castonguay et al., 2007; Cawood et al., 1994; Hames et al., 1991; Laird et al., 1993; Lin et al., 2013). The existing age constraints on the Taconic metamorphism, especially possible high-pressure metamorphism, leave open questions regarding the intensity and timing of Taconic orogenesis (e.g., Cawood et al., 1994). This, in turn, leads to debate over the collision processes (e.g., Karabinos et al., 1998; Ratcliffe et al., 1998) and the large-scale structure of this orogenic belt (e.g., De Souza and Tremblay, 2015; Macdonald et al., 2014).

In this study, we revisit the speculative high-pressure terrane in northwestern Connecticut discovered by Harwood (1975) and later studied by Maggs (1984) and Maggs et al. (1986). We investigate the petrography, mineral composition systematics, and geochemistry/geochronology of the mafic gneiss. We apply a variety of modern methods to test for eclogite facies conditions and determine the metamorphic *P–T* path, including: (1) pseudosections contoured for garnet composition, garnet mode, and reconstructed original sodic clinopyroxene compositions; (2) Ti-in-Rutile thermometry (Tomkins et al., 2007); and (3) clinopyroxene–orthopyroxene (cpx–opx) thermometry. In addition, we present new geochemical

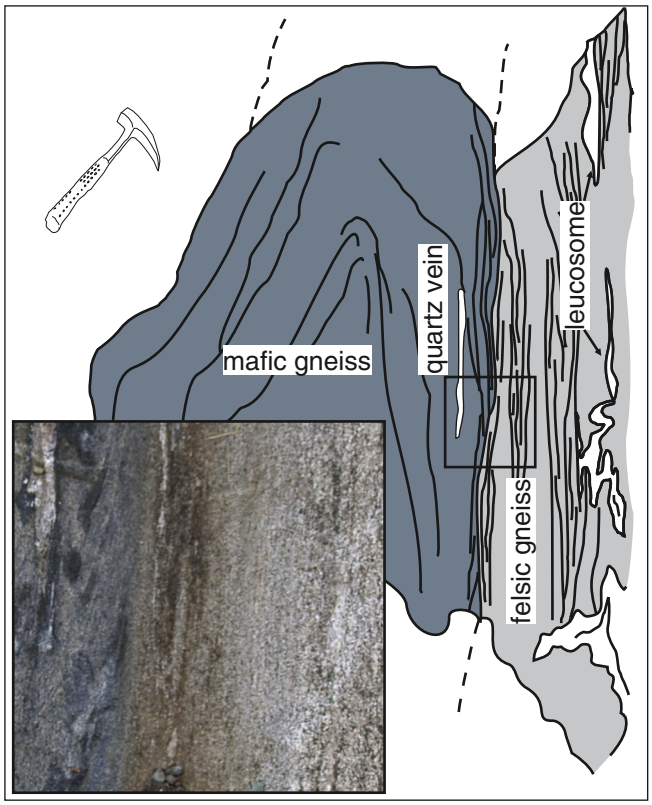


**Fig. 2.** Schematic sketch of an outcrop in the Dennis Hill State Park, Connecticut. Lenses of retrogressed eclogite are embedded in massive felsic gneisses. Inset photo shows the sheared contact.

and Secondary Ion Mass Spectrometry (SIMS) geochronological data to infer the petro-tectonic implications of the gneisses and their protoliths. The data are synthesized in a regional context to provide a timing framework for the Taconian continent–arc collision along the suture.

## 2. Geological setting

The study area is located in the Canaan Mountain Formation, a Taconic allochthonous thrust slice (Harwood, 1979b) that is in fault contact with Precambrian Laurentian crystalline basement of the Berkshire Massif (Fig. 1C). The thrust slices were transported far to the west, and were totally detached from their root zone to the east of the Berkshire Massif (Harwood, 1975; Stanley and Ratcliffe, 1985). Most of the Canaan Mountain Formation is metamorphosed arenaceous to quartzofeldspathic paragneiss. The paragneiss compositions resemble the weakly-metamorphosed Precambrian–Lower Cambrian sedimentary cover that extends to northern New England, interpreted as a transitional facies between the Dalton Formation to the west and the Hoosac Formation to the east (Gates, 1975; Stanley and Ratcliffe, 1985). The lithological similarities and the field relations of the allochthonous slices suggest that the Dalton, Canaan Mountain, and Hoosac formations are the same lithofacies telescoped into their present positions by Paleozoic thrusting (Harwood, 1979a,b).

Near the eastern thrust border with the Berkshire massif, mafic gneisses crop out sporadically as deformed, boudinaged pods and lenses (Fig. 1C). Small ultramafic bodies are also present along the thrust fault (Harwood, 1979a,b). Mafic gneisses featuring spectacular symplectic textures crop out as meter-sized oval-shaped bodies within felsic paragneiss in the Dennis Hill State Park in Norfolk, Connecticut (Fig. 2). The felsic gneiss country rock consists of quartz + plagioclase + K-feldspar + biotite ± muscovite + leucosome, and is strongly deformed. Lithologic contacts are sheared between felsic and mafic

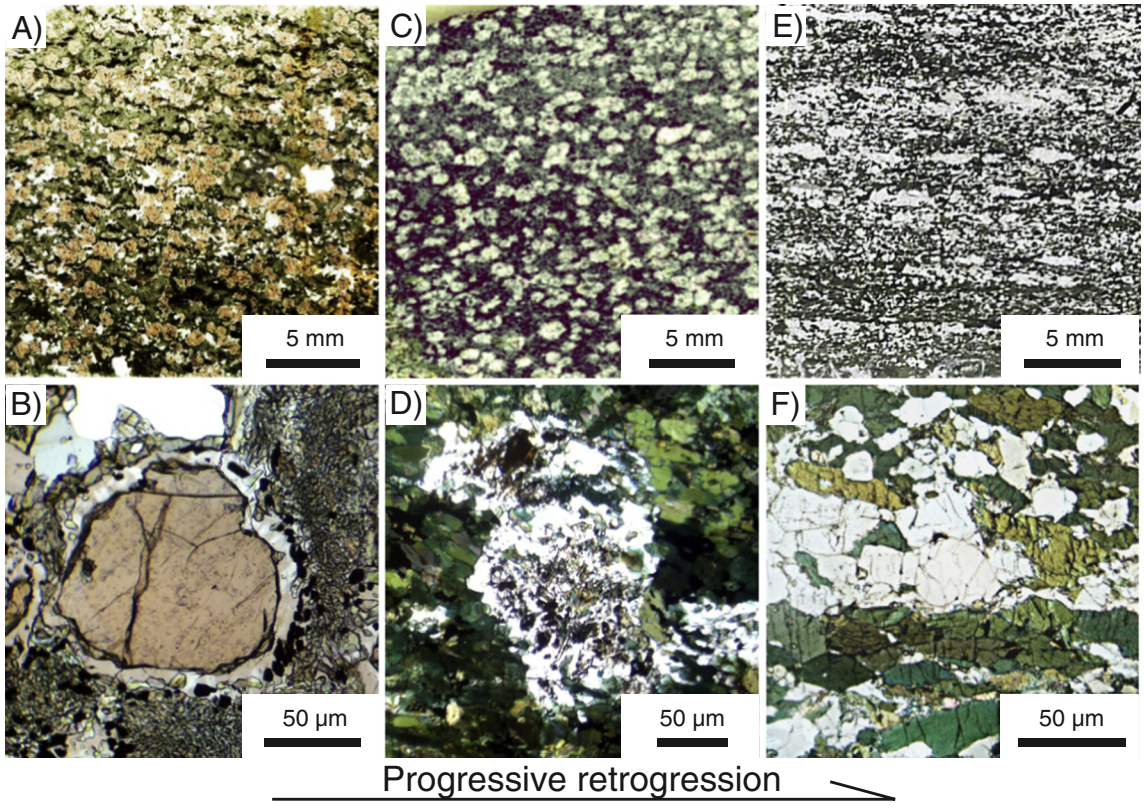


**Fig. 3.** Scanned thin sections (upper images) and corresponding photomicrographs (lower panels; plane polarized light) of microstructures in mafic gneisses of different degrees of retrogression. (A and B) Weakly retrogressed eclogite (JANW7A1), in which garnet is rimmed by plagioclase corona. (C and D) More retrogressed eclogite (JANW2A) with all garnets replaced mostly by feldspar. (E and F) Foliated mafic amphibolite (JANW3), probably retrogressed from eclogite.

**Table 1**
Abbreviation of phases and activity–composition (a–x) models used in this study.

| Phase | Abbreviation | Model system | Reference |
|---|---|---|---|
| Garnet | grt | NCFMMnASO | White et al. (2007) |
| Almandine | alm | | |
| Pyrope | prp | | |
| Spessartine | sps | | |
| Grossular | grs | | |
| Quartz | q | S | |
| Amphibole | amph | NCFMASHO | Diener et al. (2007) |
| Tschermakite | tsch | | |
| Pargasite | par | | |
| Hornblende | hb | | |
| Actinolite | act | | |
| Rutile | ru | T | |
| Biotite | bi | KFMASHTO | White et al. (2007) |
| Epidote | ep | FASHO | Holland and Powell (1998) |
| Magnetite | mt | FMATO | White et al. (2002) |
| Plagioclase | pl | NCKAS | Holland and Powell (2003) |
| Rhombohedral oxides | rhox | FMMnATO | Ghiorso and Evans (2008) |
| Ilmenite | ilm | | |
| Hematite | hem | | |
| Muscovite | mu | NKFMASH | Coggon and Holland (2002) |
| Pyroxene | px | | |
| Clinopyroxene | cpx | NCFMASO | Green et al. (2007) |
| Orthopyroxene | opx | FMASO | White et al. (2002) |
| Water | $H_2O$ | H | |

gneisses. The mafic gneiss is remarkably massive, lacks leucosomes or migmatitic textures and, thus, does not appear to have undergone any significant partial melting. Mafic gneisses displaying various degrees of retrogression also crop out in areas adjacent to Dennis Hill (Norfolk and South Sandisfield Quadrangles, Harwood, 1979a,b).

The least-retrogressed mafic gneisses contain garnets with plagioclase coronas set in a green, fine-grained matrix of symplectites (Fig. 3A, B). More retrogressed samples are rich in dark-green amphibole with only traces of clinopyroxene, indicating near-complete amphibolitization. The garnets are resorbed to different degrees. In some cases, the former presence of garnet is only marked by plagioclase feldspar-rich pseudomorphs in an amphibole-rich matrix (Fig. 3C, D). Other mafic rocks exhibit normal-looking amphibolite-facies mineral assemblages and textures, lack garnet, and are dominated by bands rich in amphibole and plagioclase (Fig. 3E and F). We infer that these banded amphibolites represent the most retrogressed equivalents of the high-pressure rocks.

## 3. Methods

Quantitative wavelength-dispersive spectrometer (WDS) analyses, energy-dispersive spectrometer analyses (EDS), and backscattered electron (BSE) imaging were carried out using the JEOL-JXA 8530F field emission gun electron probe microanalyzer (FEG-EPMA) at Yale University. Quantitative analyses employed 10 or 15 kV accelerating voltage, natural and synthetic standards, 10–20 nA (amphibole, biotite, feldspar, pyroxenes), 50 nA (garnet), or 100–150 nA (oxides) beam currents, off-

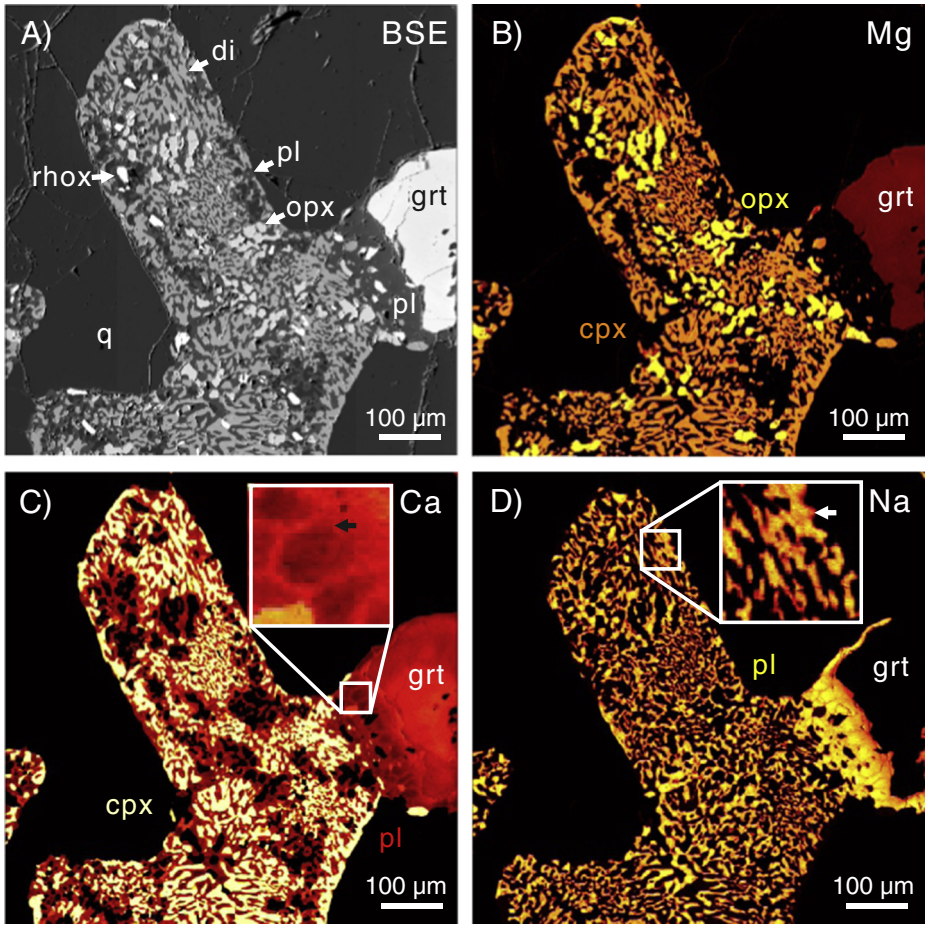


**Fig. 4.** Pseudomorph after Na-rich clinopyroxene, consisting of diopside (di) + plagioclase (pl) + orthopyroxene (opx) + quartz (q) + rhombohedral oxides (rhox). BSE image (A) and chemical maps show the texture and relative concentrations of Mg (B), Ca (C) and Na (D). Brighter colors indicate higher concentrations. The colors in different maps do not correspond to the same concentration levels. The mineral abbreviations are of the same colors as the corresponding phases in the assemblage (except for garnet). The inset zoom-in maps in (C) and (D) show the higher Ca/lower Na contents at the grain boundaries of plagioclase (arrows).

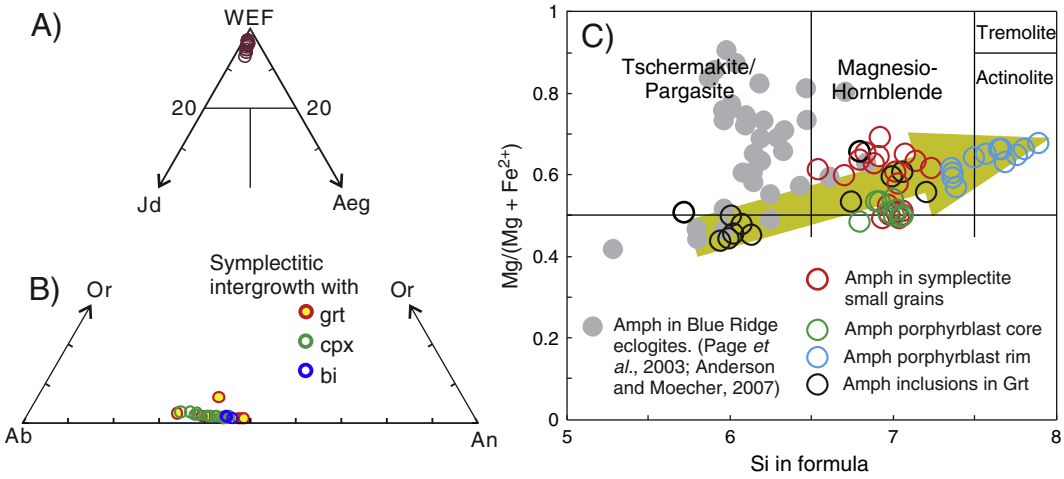


**Fig. 5.** Mineral composition diagrams: (A) clinopyroxene, (B) plagioclase, and (C) amphiboles (classification after Leake et al., 1997). The amphibole compositions of the Blue Ridge eclogites are also plotted for comparison (Page et al., 2003).

peak background corrections, $\varphi$–$\rho$–$z$ matrix corrections, and the Probe for EPMA software package. Hydrous minerals and feldspar were analyzed using a defocused electron beam (10 μm) to minimize beam damage. The chemical maps were made at 15 kV, 150 nA, and 200 ms dwell time. Trace elements in Ti ± Fe oxides were counted for long times (100–200 s on peak) to optimize counting statistics; Zr counts were obtained with a high-reflectivity PETL crystal. 10 kV was used for analyzing rutile inclusions in garnet, because of the significantly reduced activation volume relative to 15 kV. The 10 kV operation and high-brightness FEG facilitated quantitative analysis of crystals with minimum dimensions of ~800 nm. Typical analytical uncertainties for the Zr content in rutile are summarized in Ague and Eckert (2012). Mineral abbreviations are listed in Table 1.

Specimens for bulk-rock chemical analysis were cut from the rock samples (avoiding any weathered joint surfaces), abraded, cleaned with SiC paper, and sonicated in deionized water before crushing and pulverization. Analyses were done by SGS Canada Inc., Lakefield, Ontario, using X-ray florescence (XRF) for major elements and ICP-MS for trace elements. The analytical results are listed in Table A.3.

Secondary ion mass spectrometry (SIMS) analyses of zircons were performed at the University of California, Los Angeles, on the CAMECA ims 1270 using previously published techniques (Schmitz et al., 2003). Zircons were picked, separated, mounted in epoxy and sectioned. The samples were gold-coated and probed with the $^{16}O$ ion beam focused to about 20 μm spots. Concentrations of U and Th were estimated by comparing known values of $U/^{94}Zr_2^{16}O$ and $Th/^{94}Zr_2^{16}O$ in the 91500 standard (Wiedenbeck et al., 2004) to the same ratios in the unknowns. Corrections for common Pb were made using the $^{204}Pb$ proxy for samples with Th/U ≥ 0.05, and the $^{208}Pb$ proxy for samples with Th/U < 0.05. Only spot analyses with radiogenic Pb > 99% are included. Data reduction and calculation of U–Pb ages were done using the UCLA software (ZIPS v3.0.4 by C.D. Coath) and Isoplot v.4.15 (Ludwig, 2008). The age data are provided in Table A.4.

## 4. Mineral chemistry and petrography

### 4.1. Symplectites

The inferred HP assemblage preserved in the least-retrogressed mafic gneiss consists of garnet, clinopyroxene (pseudomorph), quartz, epidote, rutile and phengite (pseudomorph). Symplectite rich in diopside and plagioclase is pseudomorphous after Na-rich clinopyroxene precursors. BSE images show that the symplectite has a fine-grained texture, and consists of diopside + plagioclase + orthopyroxene + oxides + quartz (Fig. 4).

The diopside in the symplectites is relatively homogeneous in composition. Na/(Na + Ca) ratios range from 0.02 to 0.08 (Fig. 5A, Tables 2A and 2B). Lamellae of a Fe–Mg-rich phase are present in the diopside, but they are too thin to analyze quantitatively (<0.2 μm, Fig. 6A). No pristine omphacite is observed in the assemblage. Some diopside grains have been hydrated and transformed to magnesiohornblende, which tends to be idiomorphic.

Reintegration of symplectite compositions to estimate original pyroxene chemistry in previous studies suggests that decomposition reaction was largely isochemical (e.g., Anderson and Moecher, 2007; Vogel, 1966). The reintegrated composition of a representative symplectic pseudomorph in our rocks contains 27 mol% jadeite + acmite and non-trivial amounts of the Ca-Eskola and Ca-Tschermak endmembers (Table 3A). If all quartz in the pseudomorph is included, the formula of the reintegrated composition contains 2.18 Si per 6 O; the apparent Ca-Eskola (CaEs) and Ca-Tschermak (CaTs) components may be a result of Na loss during decomposition. In the less-retrogressed eclogites from the Appalachian Blue Ridge, the symplectic plagioclases show flat Ca and Na profiles from the interior of plagioclase to the grain boundaries (Anderson and Moecher, 2007). If the original plagioclases in our rocks were also unzoned, then the observed decrease in Na contents toward plagioclase grain boundaries could reflect Na loss from the symplectite (Fig. 4D). The change of $Fe^{2+}/Fe^{3+}$ ratio during omphacite

**Table 2A**
Representative pyroxene analyses (wt.%), sample JANW7B2.

| Analysis # | | $SiO_2$ | TiO2 | $Al_2O_3$ | FeO | MgO | MnO | CaO | $Na_2O$ | Total |
|---|---|---|---|---|---|---|---|---|---|---|
| 888 | Cpx sympl. | 52.83 | 0.04 | 0.88 | 7.75 | 13.75 | 0.15 | 23.37 | 0.33 | 99.18 |
| 897 | Cpx atoll | 52.28 | 0.01 | 1.03 | 11.17 | 12.18 | 0.21 | 21.97 | 0.70 | 99.56 |
| 140 | Cpx sympl. | 51.95 | 0.06 | 2.36 | 10.93 | 10.78 | 0.22 | 22.25 | 1.01 | 99.65 |
| 875 | Opx sympl. | 51.43 | 0.01 | 0.68 | 26.52 | 19.45 | 0.57 | 0.31 | 0.02 | 99.08 |
| 909 | Opx atoll | 51.35 | 0.00 | 0.48 | 27.20 | 18.37 | 0.70 | 0.38 | 0.01 | 98.63 |

**Table 2B**
Representative pyroxene structural formulas (6 O), sample JANW7B2.

| Analysis # | | Si | Ti | Al | $Fe^{3+}$[a] | $Fe^{2+}$ | Mg | Mn | Ca | Na | Mg# |
|---|---|---|---|---|---|---|---|---|---|---|---|
| 888 | Cpx sympl. | 1.980 | 0.001 | 0.039 | 0.019 | 0.243 | 0.768 | 0.005 | 0.938 | 0.024 | 0.76 |
| 897 | Cpx atoll | 1.972 | 0.000 | 0.046 | 0.015 | 0.352 | 0.685 | 0.007 | 0.888 | 0.051 | 0.66 |
| 140 | Cpx sympl. | 1.967 | 0.002 | 0.106 | 0.044 | 0.302 | 0.609 | 0.007 | 0.903 | 0.074 | 0.67 |
| 875 | Opx sympl. | 1.972 | 0.000 | 0.031 | 0.043 | 0.850 | 1.112 | 0.018 | 0.013 | 0.001 | 0.57 |
| 909 | Opx atoll | 1.991 | 0.000 | 0.022 | 0.056 | 0.882 | 1.062 | 0.023 | 0.016 | 0.001 | 0.55 |

Note: Abbreviations: sympl.: symplectite.
[a] $Fe^{3+}$ estimated based on 4 total cations per 6 O.

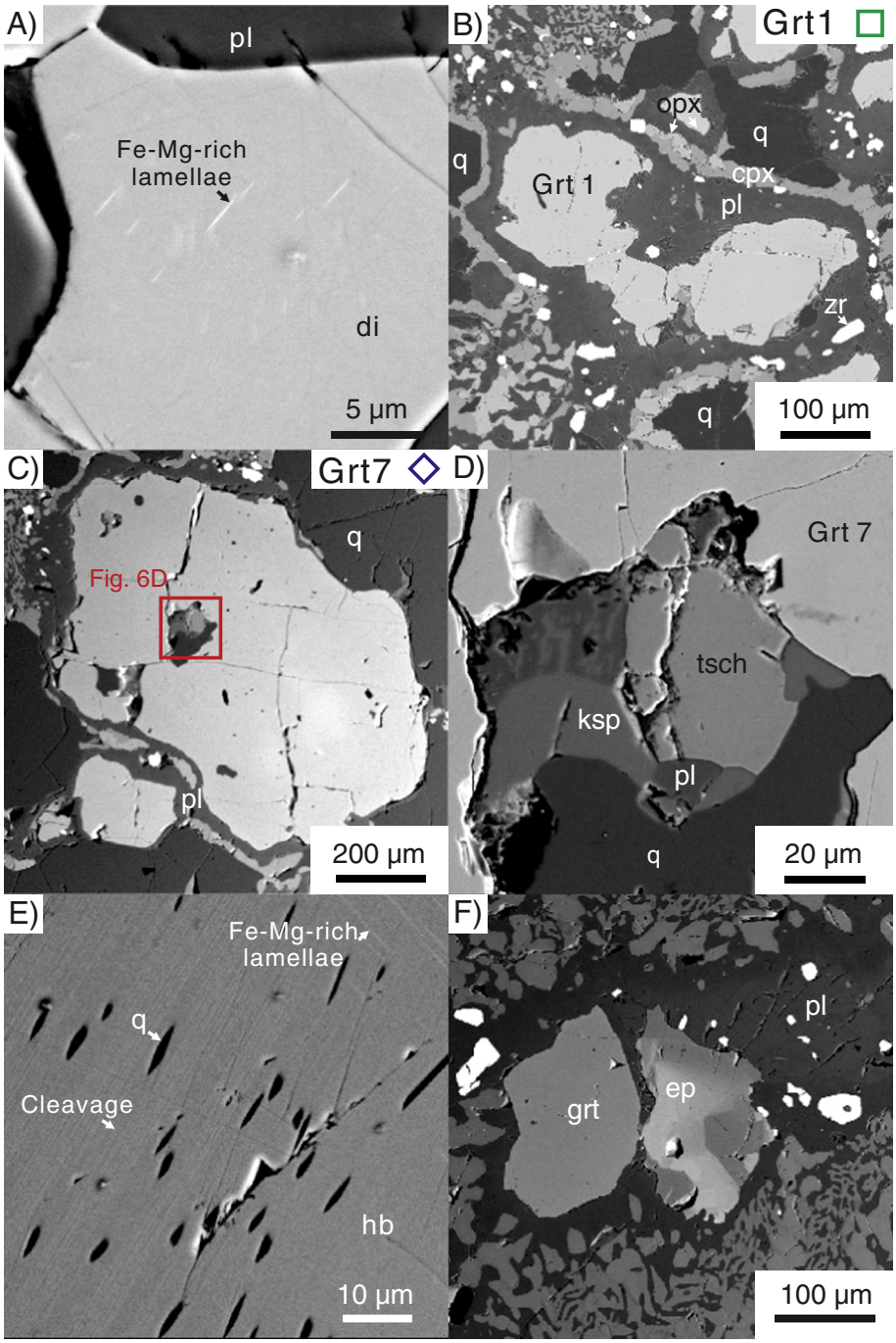


**Fig. 6.** BSE images, sample JANW7B2. (A) Exsolved Fe–Mg-rich lamellae in diopside. (B) Garnet resorption and plagioclase corona (Garnet 1); plagioclase coronas are separated from the matrix by a ring of cpx + opx. (C and D) Garnet 7 and multi-phase inclusion. (E) Oriented quartz (q) rods and Fe–Mg-rich lamellae in matrix porphyroblastic hornblende. (F) Zoned epidote with REE-rich core.

**Table 3**
Calculated compositions of re-integrated cpx–pl symplectite (in Fig. 4), assuming isochemical decomposition (except Na).

| | Quartz incorporated | | All quartz removed | |
|---|---|---|---|---|
| | Fixed $Fe^{2+}/Fe^{3+}$ | All Fe as $Fe^{2+}$ | Fixed $Fe^{2+}/Fe^{3+}$ | All Fe as $Fe^{2+}$ |
| *A. No additional Na* | | | | |
| Structural formulas (cation sum = 4) | | | | |
| Si | 2.18 | 2.18 | 2.04 | 2.04 |
| Al | 0.47 | 0.47 | 0.52 | 0.52 |
| $Fe^{3+}$ | 0.07 | – | 0.07 | – |
| $Fe^{2+}$ | 0.17 | 0.24 | 0.19 | 0.26 |
| Mg | 0.38 | 0.38 | 0.41 | 0.41 |
| Na | 0.26 | 0.26 | 0.28 | 0.28 |
| Ca | 0.47 | 0.47 | 0.51 | 0.51 |
| O | 6.32 | 6.29 | 6.22 | 6.18 |
| Excess Si in the formula | 0.15 | 0.22 | 0 | 0 |
| Endmember components (mol%) | | | | |
| Jd + Ac | 26 | 26 | 27 | 27 |
| Di + Hed | 39 | 41 | 34 | 38 |
| En + Fs | 7 | 11 | 12 | 14 |
| CaTs | 0 | 0 | 3 | 2 |
| CaEs | 28 | 22 | 24 | 19 |
| *B. Na added; no excess Al (Na = Al + $Fe^{3+}$ in formula)* | | | | |
| Structure formulas (cation sum = 4) | | | | |
| Si | 2.04 | 2.07 | 1.88 | 1.92 |
| Al | 0.44 | 0.45 | 0.48 | 0.49 |
| $Fe^{3+}$ | 0.06 | – | 0.07 | – |
| $Fe^{2+}$ | 0.16 | 0.23 | 0.18 | 0.24 |
| Mg | 0.36 | 0.36 | 0.38 | 0.38 |
| Na (added[a]) | 0.50 | 0.45 | 0.55 | 0.49 |
| | (0.26) | (0.20) | (0.29) | (0.23) |
| Ca | 0.44 | 0.45 | 0.47 | 0.48 |
| O | 6.04 | 6.07 | 5.88 | 5.92 |
| Na/(Na + Ca) | 0.53 | 0.50 | 0.54 | 0.50 |
| *C. Na added; 6 O per 4 cations* | | | | |
| Structure formulas (cation sum = 4) | | | | |
| Si | 2.02 | 2.04 | 1.94 | 1.96 |
| Al | 0.44 | 0.44 | 0.50 | 0.50 |
| $Fe^{3+}$ | 0.06 | – | 0.07 | – |
| $Fe^{2+}$ | 0.16 | 0.22 | 0.18 | 0.25 |
| Mg | 0.35 | 0.36 | 0.39 | 0.39 |
| Na (added[a]) | 0.54 | 0.50 | 0.44 | 0.41 |
| | (0.30) | (0.26) | (0.17) | (0.14) |
| Ca | 0.44 | 0.44 | 0.49 | 0.49 |
| Na/(Na + Ca) | 0.55 | 0.53 | 0.47 | 0.46 |

[a] Na added to the integrated symplectite composition.

decompression (if any) is unknown, but the varying $Fe^{2+}/Fe^{3+}$ ratios do not affect the general results.

Assuming that some Na was released during omphacite decomposition, the Na/(Na + Ca) ratio in the omphacite precursor can be estimated by imposing more constraints: (1) no excess Al (in the form of CaEs and CaTs) present in the omphacite (Table 3B) and (2) 6 oxygens per 4 cations in the pyroxene formula (Table 3C). The results for both methods indicate that about 1/3 to 1/2 of the Na might have been lost during decomposition and/or further retrograde reactions. Consequently, the Na/(Na + Ca) ratio could have been as high as about 0.5 in the clinopyroxene precursors. Although these composition integrations are semi-quantitative, they demonstrate that considerable jadeite component was likely present in the original clinopyroxene.

Symplectic intergrowths of biotite + plagioclase + oxides are almost certainly pseudomorphous after phengite or phengite + omphacite (Fig. 7; e.g., Franz et al., 1986; Janak et al., 2012; Schmädicke et al., 1992). The pseudomorphs are rimed by biotite. The biotite compositions are relatively uniform, containing up to 5 wt.% $TiO_2$ with an average Mg# of 0.56 (Tables 4A and 4B).

### 4.2. Garnet and plagioclase

We conducted chemical mapping on a representative garnet (Garnet 10, Fig. 8); the garnet is surrounded mostly by quartz which may have prevented the rim from retrogressive resorption to some extent. The compositional profiles of several other garnets are presented in Fig. A.1. The profiles of all garnets are consistent with each other.

Garnets are subhedral, 0.1–0.5 mm in diameter, and are rimmed and embayed by the polycrystalline plagioclase coronas (Figs. 6B, C, 8). Some garnets retain the outlines of euhedral cores that are easy to identify in titanium compositional maps (Fig. 8F). In garnet cores (Zones 1 and 2, Fig. 8), the $X_{GRS}$ profile is largely flat (Figs. 8A, A.1). The compositional patterns of $X_{ALM}$ and $X_{PRP}$ in the garnet cores are complicated, and reflect the prograde metamorphic history. Weak bell-shaped growth zoning of manganese (Hollister, 1966) is present in the garnet cores (Fig. 8C). Two outer zones are developed surrounding the core regions: a high-Mg/low-Ca zone (zone 3) followed by a high-Ca/low-Mg zone (zone 4; Fig. 8A, B). The highest Mg# in the inner high-Mg/low-Ca zone 3 is 0.28, and the highest $X_{GRS}$ in the outer high-Ca/low-Mg zone 4 is 0.32 (Tables 5A and 5B, probe spots labeled in Fig. 8B). Manganese is concentrated at the embayed garnet rims which represent the resorption front (zone 5; Fig. 8C; Kohn and Spear, 2000; Spear, 2014). Rim compositions are consistent among the garnet porphyroblasts and reflect equilibration with the matrix during retrograde metamorphism.

The degree of resorption varies among garnet grains. Assuming that the replacement of the garnet rims by the plagioclase corona was iso-

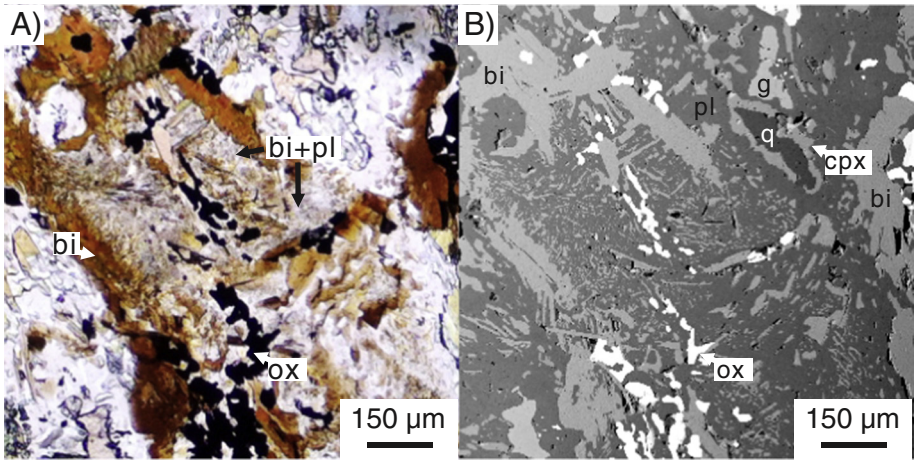


**Fig. 7.** Pseudomorph after phengite, consisting of biotite (bi) + plagioclase (pl) + rhombohedral oxides (rhox). (A) Plane polarized light. (B) BSE image.

**Table 4A**
Representative biotite analyses (wt.%), sample JANW7B2.

| Analysis # | $SiO_2$ | $TiO_2$ | $Al_2O_3$ | FeO | MgO | MnO | BaO | $Na_2O$ | $K_2O$ | F | Cl | Total |
|---|---|---|---|---|---|---|---|---|---|---|---|---|
| 917 | 35.95 | 4.99 | 15.13 | 16.80 | 12.30 | 0.08 | 0.41 | 0.06 | 9.71 | 0.11 | 0.03 | 95.67 |
| 924 | 35.85 | 4.87 | 15.21 | 16.93 | 12.34 | 0.07 | 0.44 | 0.06 | 9.57 | 0.11 | 0.04 | 95.60 |

**Table 4B**
Representative biotite structural formulas (11 O), sample JANW7B2.

| Analysis # | Si | Ti | Al | Fe[a] | Mg | Mn | Ba | Na | K | F | Cl |
|---|---|---|---|---|---|---|---|---|---|---|---|
| 917 | 2.730 | 0.285 | 1.354 | 1.067 | 1.392 | 0.005 | 0.022 | 0.009 | 0.941 | 0.047 | 0.007 |
| 924 | 2.725 | 0.278 | 1.363 | 1.076 | 1.398 | 0.005 | 0.024 | 0.009 | 0.928 | 0.047 | 0.008 |

[a] All Fe as $Fe^{2+}$.

volumetric, about 2/3 the volume of garnet has been replaced by plagioclase corona. The modes (vol. %) of garnet and garnet + corona were estimated by scanning the thin section of Sample JANW7B2, processing the image, and counting the color pixels using MATLAB (Fig. A.2; the bulk composition of this sample is also used for pseudosection analysis). We interpret the garnet + corona to represent the garnet precursor, and use their mode (22.5 vol.%) as an additional barometer to constrain the peak pressure (see below).

The plagioclase coronas are isolated from the other phases in the matrix by rings of clinopyroxene + orthopyroxene "atolls" (Fig. 6B). This feature may represent the Mg–Fe–Ca transport front when the garnet decomposes. The clinopyroxenes in these atolls are almost endmember diopside and have consistently lower Na content than those in the symplectite (Tables 6A and 6B). The plagioclase of the corona has An# ranging from 31 to 50 (Fig. 5B, Tables 6A and 6B). The An# of the corona increases toward the corona-garnet contact (Figs. 4D, 8E). We postulate that as the grain boundary of garnet retreats, the newly-formed inner part of the corona is separated from the matrix, and the addition of Ca from garnet decomposition increases the An# of the plagioclase at contacts with the relict garnet. The high An# grain boundaries might represent the paths of Ca release from the garnet to the matrix (Figs. 4C, 8E).

Plagioclase is an abundant matrix phase in the retrograde assemblage, but was unlikely to have been present in the peak assemblage; all plagioclase phases are associated with either symplectites, garnet coronas or epidote breakdown. The compositions of the plagioclases in different textural settings overlap, and have an average An# of about 40 (Fig. 5B). Rare K-feldspar and/or perthite are present as inclusions in garnet, but are not found in the matrix (Fig. 6D).

### 4.3. Hydrous phases and accessory phases

The mode of amphibole varies among rocks, depending on the degree of amphibolite-facies retrogression. Amphibole inclusions in garnets are tschermakitic and have the lowest $Si^{IV}$ = 5.65 p.f.u. (Fig. 5C; Tables 7A and 7B). These amphiboles contain higher chlorine (up to 1.24 wt.%) than those in the matrix or symplectite (Tables 7A and 7B). Tschermakitic and/or Cl-rich amphiboles are also common in the eclogites from the Appalachian Blue Ridge (Anderson and Moecher, 2007) and Newfoundland (Jamieson, 1990). The compositions of the amphiboles in the matrix plot within the magnesiohornblende field (Fig. 5C). Matrix amphiboles contain oriented quartz rods in the cores (Fig. 6E). Oriented lamellae of a Fe–Mg-rich phase (<0.2 μm) also exsolved from the matrix hornblende (Fig. 6E). The quartz rods and Fe–Mg-rich lamellae in the matrix hornblende resemble textures found in clinopyroxene from high-temperature eclogites (e.g., Anderson and Moecher, 2007; Groppo et al., 2015; Page et al., 2005). Hornblende replaced the clinopyroxene in the symplectites during exhumation, and the hornblendes in both matrix and symplectites were partially replaced by actinolite during further retrogression (Fig. 5C).

Epidote is rare in the matrix. It is chemically zoned, from REE-rich allanite cores (REE not analyzed) to low-REE epidote rims (Fig. 6F; Tables 8A and 8B). During decompression, epidote is replaced by plagioclase. The breakdown of epidote may release LREE to fluids and cause the LREE depletion of the rock compositions discussed below.

Other accessory minerals include zircon, rutile, ilmenite, and apatite. Zircon, rutile and ilmenite are present in the matrix and also as inclusions in garnet. Rutile in the matrix typically has coronas of rhombohedral oxides that exhibit exsolution lamellae of ilmenite and hematite. Both hematite lamellae in ilmenite and ilmenite lamellae in hematite are present in the assemblage; the lamella/host ratio varies from 1/6 to 1/4. The ilmenite-rich phase contains up to 10 mol% hematite component (Table A.2). The hematite-rich phase is close to endmember composition.

The mafic gneiss is cut by coarse-grained rutile–quartz–amphibole veins, in which oriented hematite planes exsolve from the rutile mega-crystals (3 × 4 cm). The solubility of rutile is low in pure water even at high pressures (e.g., Antignano and Manning, 2008), but increases significantly in Cl- or F-rich fluids (e.g., Rapp et al., 2010). The vein-hosted rutiles and the high-Cl tschermakite inclusions in garnet suggest the presence of Cl-bearing fluid at around the pressure peak.

## 5. Thermobarometry and metamorphic *P–T* path

### 5.1. Pseudosection analysis and pressure-peak condition

The pseudosection was constructed by solving non-linear equations in a MATLAB code set (Chu and Ague, 2013) with the algorithms of Powell et al. (1998), an internally-consistent thermodynamic database (Holland and Powell, 1998), and the most updated activity-composition models (summarized in Table 1). The calculated pseudosection for Sample JANW7B2 is presented in Fig. 9 (and a larger version with more labels in Fig. A.3). The rutile → rhombohedral oxide transition is pressure sensitive, and the peak-*P* assemblage contains rutile partially replaced by rhombohedral oxide. To use the rutile → rhombohedral oxides transition as a barometer, we adopt the multicomponent activity model of Ghiorso and Evans (2008) that includes ilmenite, hematite, geikielite, pyrophanite and corundum endmembers. Although this activity model was not originally derived to be consistent with the other thermodynamic data and activity models, the discrepancies among the phase equilibria are negligible (Chu and Ague, 2013).

The pseudosection is calculated in the model system NFKFMMnASHTO. The bulk-rock composition is estimated based on the X-ray florescence results (Table 9). The phase components that are not included in the activity models (e.g., K, Ti in amphibole) are subtracted from the bulk composition proportionally. The fluid is pure water and is set in excess; pseudosections for lowered water

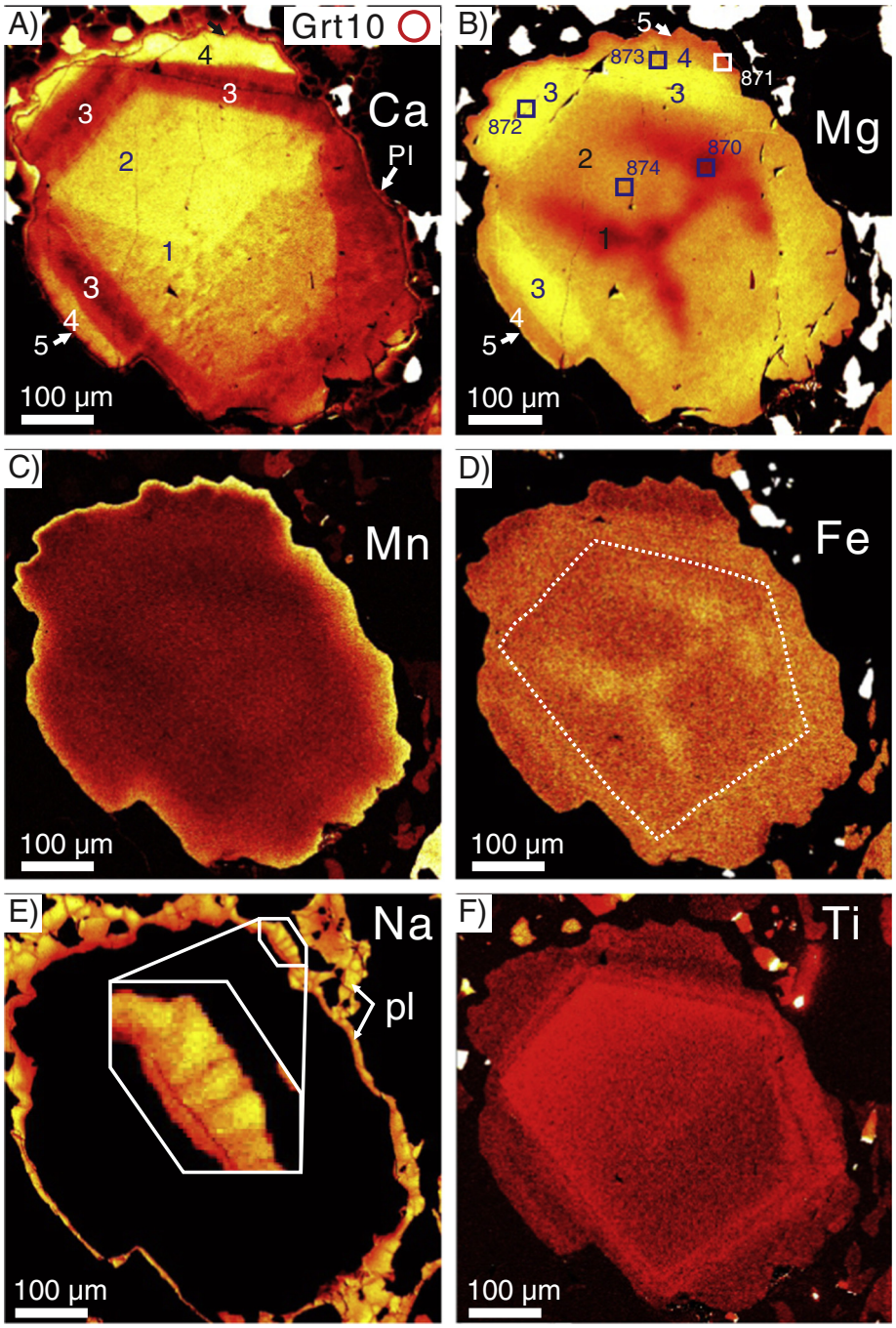


**Fig. 8.** Chemical maps showing relative concentrations of (A) Ca, (B) Mg, (C) Mn, (D) Fe, (E) Na, and (F) Ti of garnet and plagioclase corona, sample JANW7B2. Brighter colors indicate higher concentrations. Color scales in different maps do not correspond to the same element concentrations. Labeled zones correspond to numbered circles in Fig. 9. In part B, the localities of spot analyses are marked by squares and labeled with analysis numbers that correspond to Tables 5A and 5B.

activities are also discussed below. $SiO_2$ is saturated throughout the pseudosection. The precise $Fe^{3+}/Fe^{2+}$ ratio of the bulk composition is unknown, and may have varied during metamorphism, but extremely large fluid–rock ratios would have been required to change redox state significantly in these relatively oxidized rocks (Ague, 1998). Providing that most Ti and $Fe^{3+}$ reside in the oxides, and the amounts of

**Table 5A**
Representative garnet analyses (wt.%), sample JANW7B2.

| Analysis # | $SiO_2$ | $TiO_2$ | $Al_2O_3$ | FeO | MgO | MnO | CaO | $Na_2O$ | $P_2O_5$ | Total |
|---|---|---|---|---|---|---|---|---|---|---|
| 871 | 38.00 | 0.02 | 21.35 | 24.75 | 3.70 | 2.05 | 9.67 | 0.01 | 0.00 | 99.64 |
| 870 | 37.51 | 0.04 | 20.56 | 27.93 | 2.57 | 0.50 | 10.80 | 0.01 | 0.01 | 99.94 |
| 872 | 38.49 | 0.01 | 21.80 | 25.25 | 5.54 | 0.46 | 8.47 | 0.01 | 0.01 | 100.80 |
| 873 | 38.32 | 0.04 | 21.77 | 23.33 | 4.68 | 0.48 | 11.31 | 0.02 | 0.00 | 99.97 |
| 874 | 38.13 | 0.07 | 20.82 | 24.59 | 4.43 | 0.52 | 11.10 | 0.01 | 0.02 | 99.71 |

**Table 5B**
Representative garnet structural formulas (12 O), sample JANW7B2.

| Analysis # | Si | Ti | Al | $Fe^{3+}$[a] | $Fe^{2+}$ | Mn | Mg | Ca | Na | P | Mg# | $X_{GRS}$ | $X_{SPS}$ |
|---|---|---|---|---|---|---|---|---|---|---|---|---|---|
| 871 | 2.993 | 0.001 | 1.983 | 0.028 | 1.603 | 0.137 | 0.434 | 0.817 | 0.002 | 0.000 | 0.213 | 0.273 | 0.046 |
| 870 | 2.971 | 0.002 | 1.920 | 0.134 | 1.716 | 0.033 | 0.304 | 0.916 | 0.002 | 0.001 | 0.150 | 0.309 | 0.011 |
| 872 | 2.988 | 0.001 | 1.995 | 0.031 | 1.608 | 0.030 | 0.641 | 0.704 | 0.002 | 0.001 | 0.285 | 0.236 | 0.010 |
| 873 | 2.974 | 0.002 | 1.992 | 0.057 | 1.458 | 0.032 | 0.542 | 0.941 | 0.002 | 0.000 | 0.271 | 0.317 | 0.011 |
| 874 | 3.000 | 0.004 | 1.928 | 0.058 | 1.565 | 0.035 | 0.519 | 0.934 | 0.002 | 0.001 | 0.249 | 0.302 | 0.012 |

[a] $Fe^{3+}$ estimated based on 8 total cations per 12 O.

**Table 6A**
Representative feldspar analyses (wt.%), sample JANW7B2.

| Analysis # | | SiO2 | $Al_2O_3$ | FeO | MgO | CaO | BaO | $Na_2O$ | $K_2O$ | Total |
|---|---|---|---|---|---|---|---|---|---|---|
| 962 | Sympl. with bi | 59.01 | 25.79 | 0.29 | 0.11 | 8.12 | 0.05 | 6.91 | 0.26 | 100.53 |
| 964 | Garnet corona | 57.26 | 27.21 | 0.37 | 0.00 | 9.22 | 0.02 | 6.38 | 0.22 | 100.71 |
| 966 | Sympl. with px | 58.62 | 26.28 | 0.36 | 0.07 | 8.33 | 0.01 | 6.91 | 0.36 | 100.93 |
| 979 | Garnet corona | 60.91 | 24.58 | 0.14 | 0.01 | 6.16 | 0.02 | 7.97 | 0.33 | 100.13 |
| 980 | Sympl. with px | 64.20 | 22.26 | 0.21 | 0.01 | 3.78 | 0.03 | 9.44 | 0.48 | 100.40 |
| 983 | Grt incl. | 65.36 | 18.57 | 0.35 | 0.01 | 0.04 | 0.15 | 0.95 | 15.52 | 100.97 |
| 996 | Grt corona | 64.78 | 22.38 | 0.30 | 0.01 | 3.49 | 0.00 | 9.46 | 0.45 | 100.87 |

**Table 6B**
Representative feldspar structural formulas (8 O), sample JANW7B2.

| Analysis # | | Si | Al | Fe[a] | Mg | Ca | Ba | Na | K | $X_{An}$ | $X_{Ab}$ | $X_{Or}$ |
|---|---|---|---|---|---|---|---|---|---|---|---|---|
| 962 | Sympl. with bi | 2.629 | 1.354 | 0.011 | 0.007 | 0.388 | 0.001 | 0.597 | 0.015 | 0.388 | 0.597 | 0.015 |
| 964 | Garnet corona | 2.557 | 1.432 | 0.014 | 0.000 | 0.441 | 0.000 | 0.552 | 0.013 | 0.441 | 0.552 | 0.013 |
| 966 | Sympl. with px | 2.606 | 1.377 | 0.013 | 0.005 | 0.397 | 0.000 | 0.596 | 0.020 | 0.397 | 0.596 | 0.020 |
| 979 | Garnet corona | 2.708 | 1.288 | 0.005 | 0.001 | 0.294 | 0.000 | 0.687 | 0.019 | 0.294 | 0.687 | 0.019 |
| 980 | Sympl. with px | 2.830 | 1.157 | 0.008 | 0.001 | 0.178 | 0.001 | 0.807 | 0.027 | 0.178 | 0.807 | 0.027 |
| 983 | Grt incl. | 2.991 | 1.002 | 0.013 | 0.001 | 0.002 | 0.003 | 0.084 | 0.906 | 0.002 | 0.084 | 0.906 |
| 996 | Grt corona | 2.838 | 1.156 | 0.011 | 0.001 | 0.164 | 0.000 | 0.803 | 0.025 | 0.164 | 0.803 | 0.025 |

[a] All Fe as $Fe^{2+}$.

**Table 7A**
Representative amphibole analyses (wt.%), samples JANW7B1 and JANW7B2.

| Analysis # | | $SiO_2$ | $TiO_2$ | $Al_2O_3$ | FeO | MgO | MnO | BaO | CaO | $Na_2O$ | $K_2O$ | F | Cl | Total |
|---|---|---|---|---|---|---|---|---|---|---|---|---|---|---|
| 191 | Sympl. | 43.79 | 1.34 | 9.27 | 18.32 | 9.67 | 0.13 | 0.03 | 11.80 | 1.34 | 0.73 | 0.06 | 0.02 | 96.66 |
| 190 | Sympl. | 54.34 | 0.04 | 1.16 | 13.40 | 15.58 | 0.19 | 0.02 | 12.07 | 0.16 | 0.03 | 0.00 | 0.00 | 97.03 |
| 204 | Grt incl. | 36.82 | 1.45 | 18.18 | 18.46 | 6.93 | 0.09 | 0.03 | 11.40 | 2.61 | 0.32 | 0.04 | 1.24 | 97.60 |
| 929 | Matrix | 43.07 | 1.38 | 11.37 | 15.64 | 11.03 | 0.15 | 0.01 | 11.86 | 1.24 | 1.20 | 0.05 | 0.03 | 97.07 |
| 955 | Matrix | 48.91 | 0.11 | 7.29 | 13.19 | 14.56 | 0.14 | 0.06 | 11.83 | 0.76 | 0.46 | 0.06 | 0.03 | 97.49 |
| 930 | Sympl. | 46.15 | 0.72 | 9.18 | 14.68 | 12.26 | 0.12 | 0.02 | 12.08 | 0.90 | 0.78 | 0.03 | 0.03 | 96.99 |
| 936 | Sympl. | 44.57 | 0.46 | 10.67 | 15.75 | 12.04 | 0.13 | 0.00 | 11.96 | 1.15 | 0.89 | 0.09 | 0.04 | 97.79 |
| 1006 | Grt incl. | 37.38 | 0.99 | 19.51 | 17.89 | 7.27 | 0.06 | 0.03 | 10.94 | 3.07 | 0.11 | 0.08 | 0.34 | 97.74 |

**Table 7B**
Representative amphibole structural formulas, samples JANW7B1 and JANW7B2.

| Analysis # | | *T* | | $M_1$ | | | | | | $M_2$ | | *A* | | | F | Cl | Sum |
|---|---|---|---|---|---|---|---|---|---|---|---|---|---|---|---|---|---|
| | | Si | Al(IV) | Ti | Al(VI) | $Fe^{3+}$[a] | $Fe^{2+}$ | Mn | Mg | Ca | Na | Na (A) | K | V (A) | | | |
| 191 | Sympl. | 6.670 | 1.176 | 0.154 | 0.489 | 0.228 | 2.106 | 0.016 | 2.195 | 1.926 | 0.040 | 0.358 | 0.142 | 0.499 | 0.027 | 0.006 | 15.550 |
| 190 | Sympl. | 7.878 | 0.118 | 0.004 | 0.081 | 0.046 | 1.578 | 0.023 | 3.366 | 1.875 | 0.031 | 0.014 | 0.006 | 0.979 | 0.001 | 0.000 | 15.026 |
| 204 | Grt incl. | 5.645 | 2.188 | 0.167 | 1.097 | 0.389 | 1.978 | 0.012 | 1.583 | 1.872 | 0.069 | 0.705 | 0.063 | 0.230 | 0.021 | 0.309 | 16.101 |
| 929 | Matrix | 6.446 | 1.554 | 0.155 | 0.453 | 0.307 | 1.651 | 0.019 | 2.461 | 1.902 | 0.052 | 0.307 | 0.229 | 0.465 | 0.025 | 0.008 | 15.380 |
| 955 | Matrix | 7.073 | 0.927 | 0.012 | 0.315 | 0.468 | 1.127 | 0.018 | 3.138 | 1.833 | 0.089 | 0.123 | 0.085 | 0.792 | 0.260 | 0.006 | 15.196 |
| 930 | Sympl. | 6.826 | 1.174 | 0.080 | 0.427 | 0.274 | 1.542 | 0.015 | 2.703 | 1.914 | 0.046 | 0.212 | 0.148 | 0.640 | 0.014 | 0.007 | 15.280 |
| 936 | Sympl. | 6.558 | 1.442 | 0.051 | 0.409 | 0.559 | 1.379 | 0.017 | 2.640 | 1.885 | 0.061 | 0.266 | 0.167 | 0.566 | 0.040 | 0.011 | 15.383 |
| 1006 | Grt incl. | 5.634 | 2.366 | 0.113 | 1.099 | 0.374 | 1.881 | 0.008 | 1.632 | 1.767 | 0.126 | 0.771 | 0.021 | 0.208 | 0.037 | 0.087 | 15.681 |

Note: Abbreviation: sympl.: symplectite; incl.: inclusion.
[a] Cation proportions and $Fe^{3+}$ calculated considering the averages of (1) 15 cations total excluding Na and K, and (2) 13 cations total excluding Ca, Na and K (Leake et al., 1997).

**Table 8A**
Representative epidote analyses (wt.%), sample JANW7B2.

| Analysis # | $SiO_2$ | $TiO_2$ | $Al_2O_3$ | $Fe_2O_3$ | MnO | MgO | CaO | Total |
|---|---|---|---|---|---|---|---|---|
| 958 | 37.62 | 0.10 | 27.72 | 9.04 | 0.00 | 0.15 | 23.09 | 97.77 |
| 1005 | 36.75 | 0.11 | 26.75 | 8.37 | 0.03 | 0.25 | 22.07 | 94.33[a] |

[a] Epidote rim, lower total due to REE not analyzed.

**Table 8B**
Representative epidote structural formulas (12.5 O), sample JANW7B2.

| Analysis # | Si | Ti | Al | Fe[a] | Mn | Mg | Ca |
|---|---|---|---|---|---|---|---|
| 958 | 2.946 | 0.006 | 2.559 | 0.533 | 0.000 | 0.017 | 1.937 |
| 1005 | 2.974 | 0.007 | 2.552 | 0.510 | 0.002 | 0.031 | 1.913 |

[a] All Fe as $Fe^{3+}$.

exsolved ilmenite and hematite are roughly the same, we assume that the $Fe^{3+}$ to Ti ratio is 2:1 (excess 'O': Ti = 1:1, molar). In addition to the oxides, garnet, biotite and orthopyroxene contain a small amount of $Fe^{3+}$, and any variations in redox state weakly influence their stabilities. Nevertheless, the garnet Mg# and $X_{GRS}$ isopleths are largely insensitive to the bulk $Fe^{3+}/Fe^{2+}$ ratio, so the estimated $Fe^{3+}/Fe^{2+}$ ratio of the bulk composition does not affect the *P–T* estimates made herein.

The phase relations are largely pressure-dependent (Fig. 9). The hb + bi + grt + cpx + pl + rhox field occupies a large proportion of the pseudosection at 6–11 kbar. This is consistent with the garnet-bearing amphibolite-facies mineral assemblage observed in the rocks. As pressure increases, rutile becomes a stable Ti carrier at about 10–12 kbar, at the expense of rhombohedral oxide. At about 14–16 kbar, several reactions take place toward higher pressure, including the breakdown of biotite, rhombohedral oxide, and plagioclase. Amphibole is stable in a large field of the pseudosection except at high temperature and pressure, and epidote is stable at relatively high *P*/*T* conditions. Based on the phase relations, the peak assemblage inferred from the symplectite textures, grt + cpx + mu + tsch + ep + ru ± pl is stable at pressure >14 kbar (indicated by the yellow ellipse in Fig. 9). The composition of amphibole continuously evolves from tschermakite/pargasite to hornblende as pressure decreases. At pressures lower than ~6 kbar, hornblende is replaced by actinolite. Garnet, if in equilibrium with the matrix, is completely consumed at 6–7 kbar. Orthopyroxene is a stable Fe–Mg-bearing phase at temperature >800 °C at low pressures.

Representative compositional isopleths are contoured on the pseudosection for garnet and clinopyroxene (Fig. 9). The garnet Mg # (= Mg/[Mg + Fe]) isopleths are both pressure and temperature dependent; the Mg# increases toward higher pressure and higher temperature. The garnet $X_{GRS}$ isopleths depend on both *P–T* conditions and the phase assemblage. In the epidote-free fields, the garnet grossular proportion decreases as temperature increases and/or pressure decreases. In the area where epidote is stable and competes for Ca, garnet $X_{GRS}$ decreases toward higher pressure where more epidote phase is present in the assemblage. The garnet isopleths of the outer Ca-rich overgrowth zone (e.g., Zone 4 in Garnet 10, Fig. 8) intersect at about 13 kbar, 735 °C. The more resorbed garnet (e.g., Garnet 1, Figs. 6B, A.1) records lower pressure. The Na/(Na + Ca) isopleths of clinopyroxene are subparallel to the temperature axis. The Na/(Na + Ca) ratio increases toward higher pressures.

The chemically zoned garnets indicate disequilibrium during metamorphism, so we need to consider the effective bulk composition due to the fractionation of components into the core of garnet (e.g., Evans, 2004; Spear, 1988). Thus, we remove the garnet core components (Zones 1 and 2, Fig. 8) and recalculate the phase equilibria and isopleths (Fig. A.4). For the garnet-bearing assemblages, the phase equilibria and garnet isopleths are fairly insensitive to the change of the bulk composition away from the garnet-out boundary. The isopleths corresponding to the garnet rim compositions intersect on the garnet-out boundary at 745–770 °C, 8 kbar in the garnet-core-removed pseudosection. These

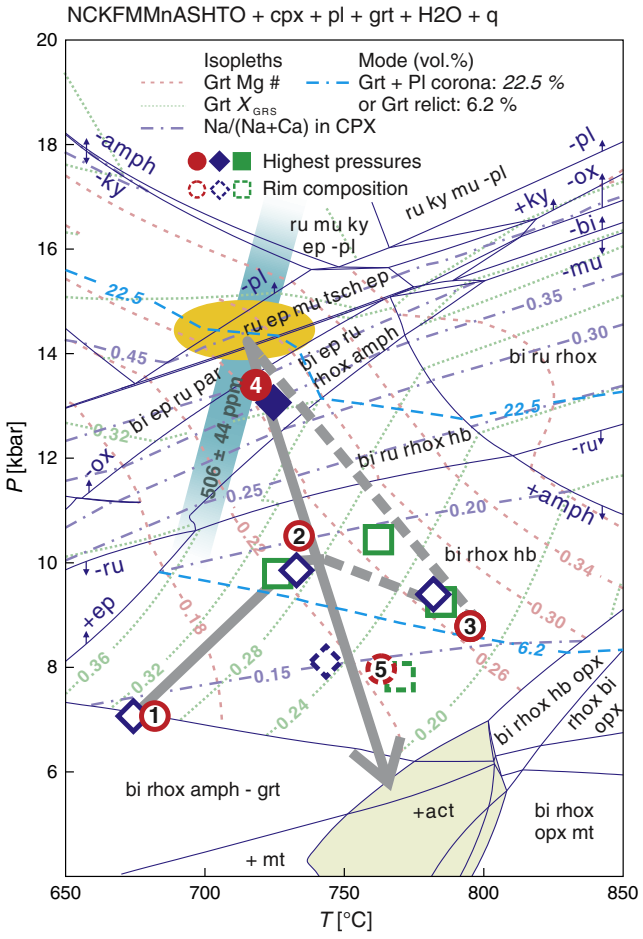


**Fig. 9.** *P–T* pseudosection for sample JANW7B2 (see Fig. A.3 for larger version). Isopleths of garnet Mg# (= Mg/[Mg + Fe], dashed red curves), grossular component (dotted green curves), and Na/(Na + Ca) ratio in clinopyroxene (dash-dot purple curves) are overlain. *P–T* conditions corresponding to the garnet compositional profiles are plotted: circles for Garnet 10 (Fig. 8, with the corresponding zone numbers labeled), and diamonds and squares for two other garnets in the same sample (Garnets 1 and 7; Figs. 6B, C, A.1). Garnet rim compositions (dotted symbols) are plotted using effective bulk composition calculated with garnet core components removed (Fig. A.4). Garnet mode and garnet + corona mode are plotted as blue dashed lines. Blue band is a *P–T* curve (±2σ) based on Zr-in-rutile thermometry (Tomkins et al., 2007). Yellow ellipse is inferred peak-*P* condition based on garnet composition zone 4 (filled symbols), tschermakite amphibole inclusions in garnet, garnet + corona mode, reintegrated omphacite composition, phengite and rutile (without rhombohedral oxide) in the peak-*P* assemblage, and Zr-in-rutile thermometry. Thick-gray curve is the inferred *P–T* path.

*P–T* conditions are plotted as representative of the garnet rims in Fig. 9. More complicated garnet-growth simulation is of course possible, but we reasonably conclude that the influence of effective bulk composition on the *P–T* estimates made in the study is minor.

The garnet proportion increases markedly toward higher pressure, in response to the decomposition of plagioclase and amphibole. The garnet proportion is used as a barometer in previous studies including Nahodilová et al. (2011), Štípská et al. (2014), and Lang and Gilotti (2015). We counted the modes of garnet and garnet + corona, and use the latter to estimate the mode of garnet at peak conditions assuming isovolumetric decomposition. The garnet + corona mode contour (22.5 vol.%) lies at 14–14.5 kbar at 700–750 °C in the field of the peak

**Table 9**
Bulk-composition used in the pseudosection (sample JANW7B2, mol %).

| $SiO_2$ | $TiO_2$ | $Al_2O_3$ | FeO | MgO | MnO | CaO | $Na_2O$ | $K_2O$ | O |
|---|---|---|---|---|---|---|---|---|---|
| 52.07 | 1.71 | 8.66 | 11.54 | 9.50 | 0.18 | 11.20 | 3.10 | 0.33 | 1.71 |

assemblage, which agrees well with the isopleths of garnet and clinopyroxene. We note here that the calculated 'mode' in this context denotes the volume proportion of a phase in the total volume of *solid* phases.

The available activity models cannot fully represent the observed mineral compositions: the clinopyroxene model does not include the CaTs endmember, and the amphibole model does not include K, Ti, or Cl. Those effects are largely unknown, but are considered limited (Štípská et al., 2014). No melt model of the mafic composition is available. The temperature of the pressure-peak (~710 °C), is on, or only slightly higher than, the water-saturated solidus for epidote-bearing amphibolite (Ellis and Thompson, 1986; Schmidt and Poli, 2004). The temperature-peak phase relations may not be as well constrained, but the main concern of this study is the pressure-peak conditions. If the rock underwent partial melting, the process must have been incipient and localized, as the rocks are massive and lack leucosomes. In addition, the high-Cl amphibole inclusions in the garnet suggest high-salinity fluid that would have lowered the activity of water ($a_{H_2O}$) and increased the solidus temperature to some degree.

In sum, the phase relations, garnet Mg# and $X_{GRS}$ isopleths, clinopyroxene Na/(Na + Ca) isopleths, and the garnet + corona mode contours together indicate a peak pressure in excess of 14 kbar at 700–750 °C. Further temperature constraints are discussed below.

### 5.2. Zirconium-in-rutile thermometer

We apply the pressure-dependent Zr-in-Rutile thermometer calibrated by Tomkins et al. (2007). The successful application of the thermometer requires that both zircon and quartz are saturated in the system (Tomkins et al., 2007; Watson et al., 2006; Zack et al., 2004). The metabasites contain quartz in the matrix and are cut by quartz veins. Quartz inclusions are also widespread in garnet. Zircons are present in the matrix and as small inclusions in garnet. If Zr is undersaturated, or the zircons contain significant amounts of impurities, the temperature estimated using Zr-in-rutile thermometry is a lower limit.

The representative rutile EPMA data and details of data analyses are presented in Table A.1. The Zr contents exhibit two major peaks in the histogram (Fig. A.5): 164 ± 18 ppm and 506 ± 44 ppm (±2σ). Generally the rutiles in the matrix or included at the garnet rims contain less Zr, but no systematic variation in rutile Zr content from core to rim in garnet is present (Fig. A.5). This might be due to the heterogeneous concentration of Zr in garnet, sluggish Zr diffusion in garnet, and/or selective retrogression of rutile connected to the matrix by cracks.

We infer that the low-Zr rutiles correspond to the retrograde stage, which might reflect rutile precipitation at successively lower temperature (~584 °C at 5 kbar), or Zr lost by diffusion through cracks in garnet. Resetting of rutile Zr contents has been documented elsewhere (e.g., Ague et al., 2013; Luvizotto and Zack, 2009). The medium-Zr group yields about 710 °C at 14 kbar, and probably indicates the temperature of the pressure peak. Two analyses have higher Zr concentrations (887 ± 63 ppm) that yield the highest temperature estimate (735 °C at 8 kbar); this is consistent with either prograde heating or exhumation (Fig. 9).

### 5.3. Clinopyroxene–orthopyroxene thermometer

The partitioning of Fe and Mg between coexisting ortho- and clinopyroxene is temperature sensitive:

$$MgSiO_3 + CaFeSi_2O_6 = FeSiO_3 + CaMgSi_2O_6$$

Coexisting ortho- and clinopyroxene are present in the symplectite, but the orthopyroxene is only stable at high temperature (>800 °C) and low pressure (<7–9 kbar) in the water-saturated pseudosection (Fig. 9). The metamorphic *P–T* path is likely outside the stability field of orthopyroxene (see below). In addition, the presence of chemical variations in clinopyroxene within symplectites suggests that the assemblages are not in full local equilibrium. Nevertheless, local Fe–Mg exchange equilibrium might be reached between the fine-grained pyroxenes in the symplectic intergrowth, and record the temperatures during the retrograde metamorphism. The thermometer is calculated using the same data set and activity models as in the pseudosection.

The compositions of symplectite orthopyroxenes are largely constant, but the Mg# of the clinopyroxene varies over a large range. The high-Na clinopyroxenes (Na > 0.05 p.f.u.) have Mg# as low as 0.63 and would indicate unrealistic temperatures >1000 °C if in equilibrium with the orthopyroxene. We use the average compositions of only the low-Na clinopyroxenes and assume local equilibrium with the orthopyroxene in each symplectite.

The highest temperature calculated using the thermometer is at about 775 °C (Fig. A.6), and is broadly consistent with the post-peak-*P* temperature indicated by the garnet rim isopleths in the pseudosection (Fig. 9). The other temperature estimates are lower, and suggest continuous Fe/Mg exchange between the pyroxenes during cooling.

### 5.4. Metamorphic P–T path

The pressure peak is inferred to have occurred in the grt + cpx + mu + ep + ru + tsch stability field at about 710 °C, >14 kbar. In this section, we use the garnet compositional zoning and associated phase assemblages to construct a likely *P–T* path.

The compositional zoning pattern of the garnet core reflects a heating path along a 20–25 °C/km geotherm (1 → 2 in Fig. 9). The Mg# troughs in the garnet cores (Zone 1, Figs. 8B; A.1) correspond to 675 °C, 7 kbar, close to the garnet-in boundary in the pseudosection (Fig. 9). The higher Mg# regions of the garnet core (zone 2, Fig. 8B) indicate *P–T* conditions of about 745 °C, 10 kbar.

Two outer compositional zones (Zones 3 and 4 in Fig. 8) surround the euhedral garnet core that has sharp boundaries in the chemical maps (Fig. 8). The inner high-Mg, low-Ca growth zone 3 (Fig. 8) corresponds to an increase in temperature, and/or a decrease in water activity by partial melting. The peak temperature is lower than 800 °C, and is not well constrained.

Additional pseudosections were calculated in the *P–T* range 700–820 °C, 7–11 kbar to assess the possible effects of lowered water activities, partial melting, or high salinity fluid on the phase assemblage and garnet isopleths (Fig. A.7). When the water activity is lowered, the high-Mg/low-Ca Zone 3 in garnets (Fig. 8) is stable at somewhat lower temperatures, and opx is stable over a larger *P–T* range. For $a_{H_2O} = 0.7$, the temperature shifts of the isopleths are as much as 50 °C, and the "peak temperature" becomes almost identical to the highest temperature indicated by the garnet core (Zone 2 in Figs. 8, A.7). Thus the high-Mg Zone 3 (Fig. 8) might correspond to either an increase in temperature or decrease in water activity. The preferential sequestration of Fe in partial melt might also affect the garnet isopleths, but the effect is difficult to estimate without a proper melt activity model.

The outer high-Ca zone 4 (Fig. 8) records ~13 kbar, coexisting with the epidote-bearing assemblage. Nevertheless, this zone has been resorbed and modified during the decompression stage and, thus, reflects a pressure lower than the actual pressure peak. Pristine omphacite is not preserved, but the inferred Na/(Ca + Na) ratio of the original Na-rich clinopyroxene is higher than 0.45, corresponding to pressure higher than 14 kbar at 700–750 °C. The peak pressure was 14–15 kbar as constrained by the garnet compositional isopleths, muscovite (phengite) breakdown reaction, the mode of garnet + corona, the tschermakite inclusions in garnet, the reintegrated omphacite composition, and the presence of rutile as the sole HP oxide (Fig. 9). We infer that the Zr-in-rutile thermometer (Tomkins et al., 2007) yields the temperature at peak pressure (~710 °C; Fig. A.5).

Garnet was absorbed to varying degrees during decompression and replaced by multicrystalline plagioclase coronas. The garnet zone 4 of

high-pressure growth is only rarely preserved (e.g. Fig. 8). The contours of garnet mode in the pseudosections are pressure sensitive (Figs. 9, A.7). The mode of relict garnet (6.2 vol.%, Fig. A.2) indicates pressures of 8–10 kbar, consistent with the amphibolite facies retrogression. The isopleths for the garnet rims intersect at 745–770 °C, 8 kbar in the garnet-core-removed pseudosection (Fig. A.3), agreeing well with the measured mode of relict garnet.

The growth zone developed at the high-temperature stage (Zone 3) is mostly preserved (Figs. 8, A.1). The garnet mode of the peak-temperature assemblage approaches or is slightly smaller than the garnet mode of the retrograde assemblage (6.2 vol.%). The garnet-mode barometer demonstrates that the temperature peak was reached at relatively low pressures, and that the transition from the temperature peak (Stage 3 in Fig. 9) to the pressure peak required a strong pressure increase (5–6 kbar). The garnet mode of the peak-temperature assemblage is higher if the water activity is lowered (~10 vol.% with $a_{H2O} = 0.7$), but is still significantly smaller than the garnet mode of the peak-pressure assemblage (22.5 vol.%). A pressure change is the only way to significantly affect the garnet mode for this assemblage (Figs. 9, A.7); thus, the garnet growth-resorption history indicates that the rocks underwent compression and decompression processes.

The predicted trend of amphibole evolution along the decompression path (tschermakite → hornblende → actinolite) is also qualitatively consistent with the textural observations. Tschermakites are present in the peak-*P* assemblage as garnet inclusions. We infer that the oriented quartz rods in the matrix amphiboles (Fig. 6E) are a relict texture of tschermakite formation during the compression process (3 → 4 in Fig. 9); tschermakite was less siliceous so that silica exsolved. During decompression, the matrix amphibole transformed back to hornblende, but preserved the exsolution texture indicating its tschermakite precursor. Consequently, the quartz rods in amphiboles are another indicator of HP conditions.

The peak pressure of 14–15 kbar corresponds to 50–55 km depth if the pressure was largely lithostatic. Given that the host formation is a ductilely-deformed thrust slice, viscous heating and tectonic overpressure may have also contributed to the heating and compression (Schmalholz and Podladchikov, 2013). After the pressure-peak, the eclogite-facies assemblage underwent amphibolite facies overprinting during near-isothermal decompression.

## 6. Protolith geochemistry

The least-retrogressed samples are used to discuss the geochemical characteristics of the protoliths. The mafic gneisses have variable rare earth element (REE) abundances, but all have similar light REE (LREE) enrichment and little-fractionated heavy REE (HREE) (Fig. 10A), with normalized La/Yb = 2.94–5.18, La/Sm = 1.51–2.33, Gd/Yb = 1.70–1.84, and a Σ REE concentration of 110 to 220 ppm. Eu anomalies are small to nonexistent. The general REE patterns resemble those of ocean–island basalt, but have elevated HREE contents that may reflect a shallower origin of the mafic magma (Rollinson, 1993). In the primitive-mantle-normalized trace element spidergram (Fig. 10B), mafic gneisses have variably depleted water-soluble large-ion lithophile elements (LILEs), such as Rb, Ba, K and Sr, likely an effect of metamorphic dehydration. Two samples (7B and 8B) with consistently lower trace element contents may be due to metamorphic alteration or protolith variability.

The chemical compositions of the mafic rocks were possibly modified during metamorphism, particularly as elements are likely more mobile at higher pressures (e.g., Antignano and Manning, 2008; Konrad-Schmolke et al., 2011; Manning, 2004). Relatively immobile elements must be identified to infer the igneous origin. Zr has low solubility in lithospheric fluids (Ague and Nicolescu, 2014; Ayers and Watson, 1991; Bernini et al., 2013; Breeding et al., 2004), and is chosen as a reference to explore the relative mobility of the other trace elements.

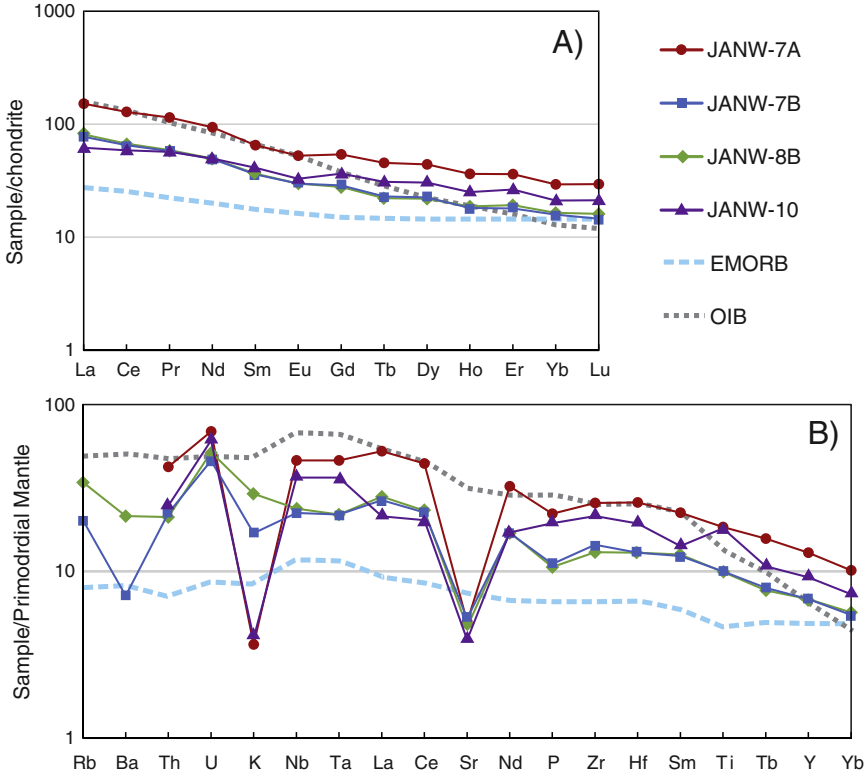


**Fig. 10.** (A) Chondrite-normalized rare earth elements patterns and (B) primitive mantle-normalized trace element patterns for mafic gneiss. Values for chondrite and primitive mantle abundances are from Sun and McDonough (1989). The profiles for average ocean–island basalts (OIB) and E-MORB (Sun and McDonough, 1989) are also plotted for reference.

Geochemical discrimination diagrams usually use the ratios of element concentrations instead of the absolute values. Thus, as long as the ratios remain constant during metamorphism, they are diagnostic of petrotectonic origins. The bivariate plots between the elements of interest and the reference Zr are presented in Fig. A.8. Linear correlations indicate that the variations in concentrations were due to primary igneous processes or some degree of rock mass loss or gain of mobile elements during metamorphism (Ague, 1994). Although the high-field strength elements (HFSEs) might be mobile during high-pressure metamorphism (e.g. Gao et al., 2007), their ratios against Zr are largely constant, as are those of the HREEs. In contrast, the La/Zr ratio varies among the samples, suggesting some decoupling of LREE and Zr behavior. Given the above, we did not use discrimination diagrams involving LREEs and LILEs.

The discrimination diagrams (Fig. 11) all indicate within-plate characteristics for the mafic gneiss. Regional mapping shows that the eclogite and equivalent amphibolites were likely dikes in the felsic gneiss (Harwood, 1979a,b; Maggs, 1984). The field relations and the geochemistry of the mafic gneisses suggest that they were originally rift-related dikes intruded into the passive margin of Laurentia.

## 7. Geochronology

Zircons from the felsic gneiss are euhedral to subhedral, yellow to honey-color grains. The textural and chemical features of the sectioned grains are associated with an early igneous origin and later growth/recrystallization. The cores of zircons have Precambrian ages and high U/Th ratios (>0.1). Some detrital cores of zircons are characterized by oscillatory zoning (Fig. 12A), and some are featureless (Fig. 12B). The cores of detrital zircons from the felsic gneisses yield ages from 856 to 1282 Ma, statistically peaked around 1134 and 967 Ma (Fig. 13A). The 1134 Ma peak broadly corresponds to Grenvillian tectonomagmatic events (Rivers, 1997). The younger group is coincident with the age of post-orogenic granites in the Green Mountain and Berkshire Massifs (Karabinos and Aleinikoff, 1990). The age pattern of the detrital cores confirms the Laurentian origin of the Canaan Mountain Formation.

The metamorphic rims of the zircons in the felsic gneisses are homogeneous and dark in the BSE images, and have significantly lower Th/U ratios (<0.05) than the igneous cores (Fig. 12A, B). The spot analyses on the metamorphic rims yield a concordant age of 456 ± 11 Ma (2σ uncertainties here and below; Fig. 13B).

Zircons from the mafic gneiss are anhedral, round, clear, and glassy. They are much smaller than those from the felsic gneiss. Zircon xenocrysts of Grenvillian ages are present in the mafic gneiss (Fig. 12C), suggesting an intrusive relationship between the mafic dikes and the felsic country rocks.

Several high (>0.1) Th/U ratio core spot analysis sites yield ages ca. 530 Ma (Fig. 12D), which are interpreted as the magma intrusion age (three shaded data rows in Table A.4A; concordia age 529 ± 22 Ma). Such cores are rare, and their oscillatory zonation is weakly developed but still clearly discernable (Fig. 12D). The last major pulse of breakup-related magmatism on the Laurentian margin ceased at around 550 Ma (Burton and Southworth, 2010 and references therein), but extension continued into the Early Cambrian (Allen et al., 2009; Lavoie et al., 2003). For example, syn-rift slope deposits in southern Québec contain late Early Cambrian fauna (Lavoie et al., 2003). In New England, the Early Cambrian Cheshire Quartzite (~530 Ma) overlies the syn-rifting succession and postdates the rifting event (Osberg, 1969). The mafic protolith age for the Connecticut eclogite (ca. 530 Ma) also corresponds broadly to the Cambrian aulacogen in Oklahoma (539–528 Ma, Hames et al., 1998; Lambert et al., 1988).

The metamorphic zircons or zircon growth zones from the mafic gneisses are homogeneous and either dark or bright in BSE images. Small metamorphic zircons (20–30 μm) were analyzed to obtain the

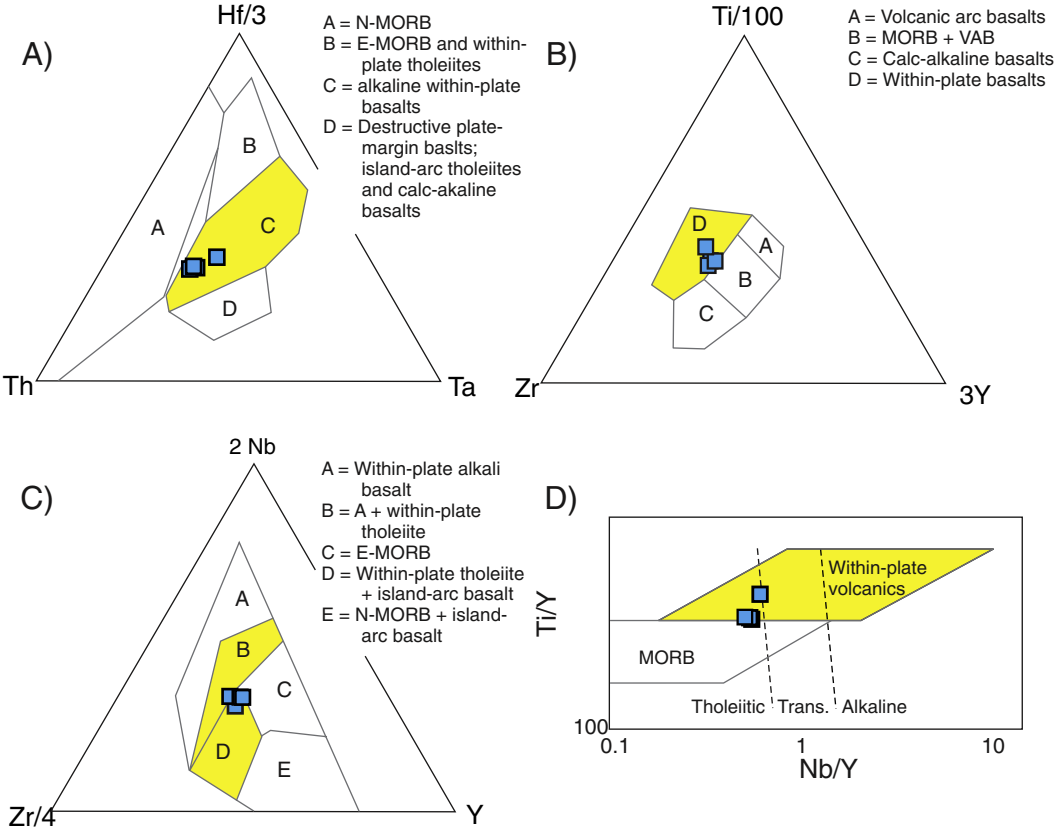


**Fig. 11.** Geochemical discrimination diagrams for mafic gneisses. (A) Th–Hf–Ta diagram (Wood, 1980); (B) Ti–Zr–Ti diagram (Pearce and Cann, 1973); (C) Zr–Nb–Y diagram (Meschede, 1986); (D) Ti/Y–Nb/Y diagram (Pearce, 1982). The data points cluster in the highlighted zones.

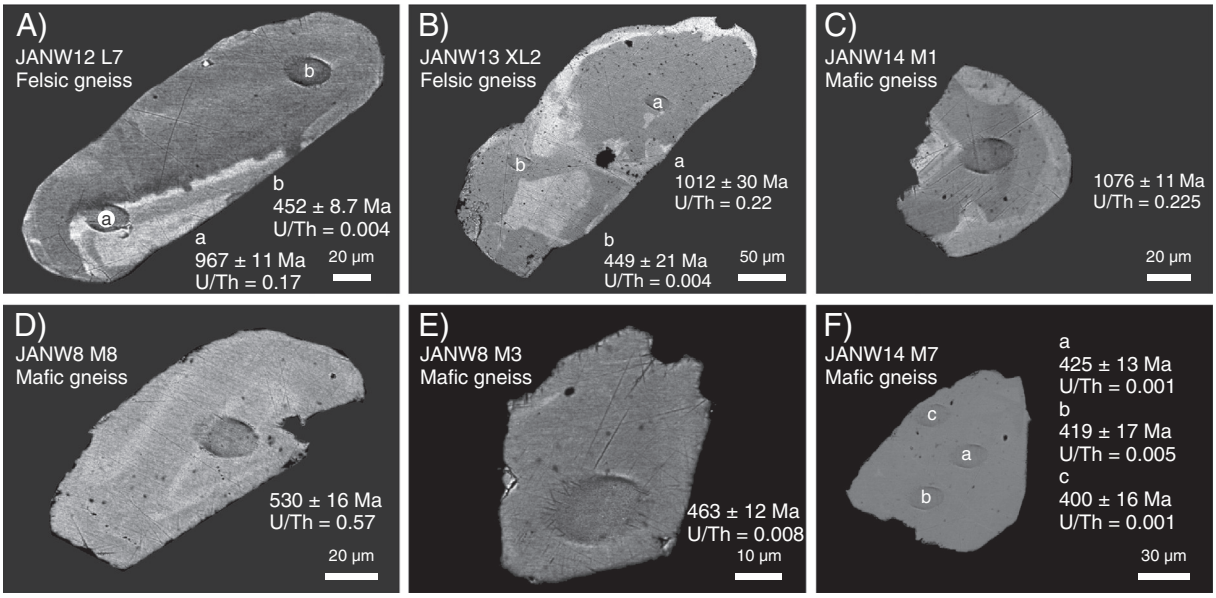


**Fig. 12.** BSE zircon images. Zircons from felsic gneiss host rocks (A–B) showing (A) oscillatory detrital core and thick metamorphic overgrowth rim, and (B) more irregular core–rim structures. (C–F) Zircons from mafic gneiss illustrating (C) Grenvillian xenocryst, (D) oscillatory zoning in zircon of Cambrian age with igneous origin, (E) homogeneous, featureless metamorphic zircon of Taconian age and (F) featureless metamorphic zircon of Acadian age (1σ uncertainties).

metamorphic age (Fig. 12E). These zircons are dark, homogeneous and featureless in BSE images, and have low U/Th ratios (<0.01). They yield an average age of 456 ± 4.6 Ma (Fig. 13C), indistinguishable from the metamorphic zircons in the felsic host gneiss.

An important question is whether the 456 Ma metamorphic age corresponds to the peak temperature, the peak pressure, or some combination. The preserved sharp garnet compositional zoning suggests an extremely short duration of metamorphism (Fig. 8). For comparison, the diffusion length scale at the garnet core–rim compositional contrast is less than 10 μm for the garnets from the mafic gneiss, whereas 1 Ma of diffusion in a Barrovian garnet at 660 °C leads to a length scale of about 100 μm (Ague and Baxter, 2007; Chu and Ague, 2015). Thus, the duration of high-*T* conditions (>660 °C) for the Connecticut eclogite was shorter than 1 Myr. The timescales and their implications deserve further investigation, but the comparison clearly demonstrates that the timing of the peak-*T* and peak-*P* stages is indistinguishable using U–Pb dating. Thus, it is reasonable to conclude that the 456 ± 4.6 Ma metamorphic age reflects eclogite facies metamorphism within the analytical uncertainties. Evidence for fast tectono-metamorphic events has been found elsewhere in the orogen; identical muscovite and hornblende $^{40}Ar/^{39}Ar$ ages in a sample (ca. 466 Ma; Castonguay et al., 2014) suggest very rapid exhumation of the Humber margin.

If a high temperature zircon overprinting event occurred after the decompression, the duration of the high temperature conditions must still have been short (<1 Myr) and within the uncertainty of the 456 ± 4.6 Ma U–Pb age. Otherwise the sharp chemical zonation of garnet would have been erased. In addition, any lower temperature metamorphic activity (<650 °C) is extremely unlikely to have entirely reset the U–Pb ages of zircons (e.g., Vorhies et al., 2013), so we discount this possibility. Furthermore, we note that diffusion in garnet is very sluggish at temperatures less than ~550–600 °C and, thus, greenschist to lower amphibolite facies retrograde overprinting (see below) would have had little impact on the prograde garnet growth zoning.

The new metamorphic age of 456 Ma is consistent with previous geochronological studies in southern New England and southeastern New York. Staurolite from the Taconic allochthon Walloomsac Formation in New York yields a U–Pb age of 454 ± 6 Ma (Lanzirotti and Hanson, 1997). Previous researchers have conducted extensive K/Ar and $^{40}Ar/^{39}Ar$ dating of the Precambrian basement in the area, but most of the Paleozoic data yields Silurian or younger ages (summarized

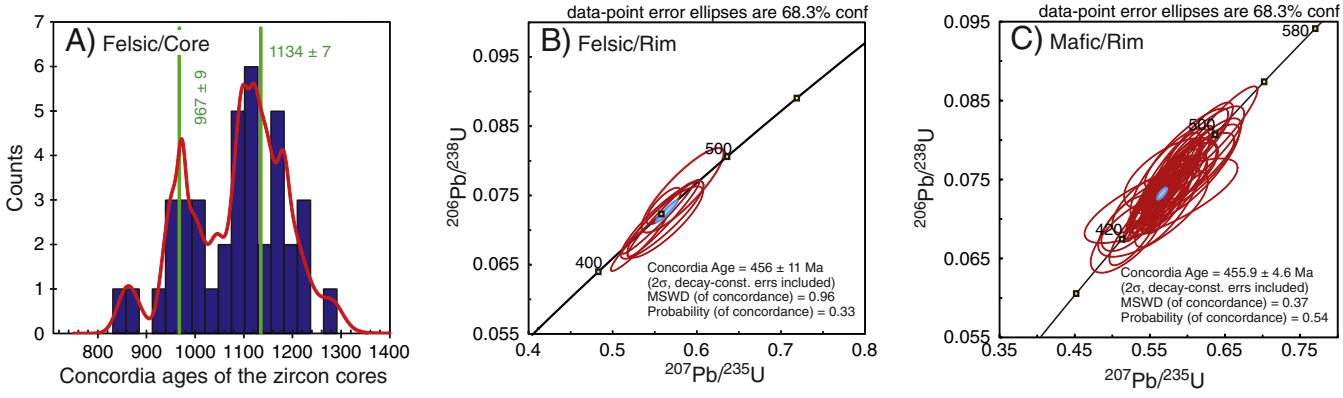


**Fig. 13.** Results of zircon U–Pb dating. (A) Histogram showing the distribution of concordia ages for the metamorphic zircon cores from the felsic gneiss. The core ages are statistically peaked at 967 ± 9 Ma and 1134 ± 7 Ma (2σ). (B and C) Concordia diagram showing spot analyses on metamorphic zircon rims from the felsic host rock (B) and the mafic gneiss (C). Error ellipses are plotted at 1σ. Concordia ages indicated in Ma.

by Laird, 1988; Laird et al., 1993; Sutter et al., 1985). Dallmeyer (1975) and Dallmeyer and Sutter (1976) reported 483–463 Ma total fusion ages from the metamorphosed Precambrian basement in New York; we recalculate these and obtain the plateau ages of 451 ± 6 and 462 ± 6 Ma based on the reported step-heating data in the original papers (Fig. A.9). Sutter et al. (1985) obtained 466 ± 5.1 and 446 ± 6.2 Ma hornblende plateau ages in the Berkshire Massif of western Massachusetts, and Hames et al. (1991) reported hornblende ages as old as 446 ± 7 Ma in the Housatonic Massif of Connecticut.

The very outermost portions of some zircon grains from both felsic and mafic gneisses are bright in BSE images, but are too narrow for spot analysis. The spot analyses overlapping the bright rims give mixed ages of Taconic and overprinting events, and are thus discarded. Rare homogeneous metamorphic zircons of post-Taconic, broadly Salinic–Acadian ages are also found in the mafic gneiss (Fig. 12F). These are consistent with a hornblende $^{40}Ar/^{39}Ar$ age of 416 ± 3 Ma for the Canaan Mountain Formation (Hames et al., 1991), reflecting closure at ~550 °C (Harrison, 1982) or new amphibole crystallization at or below this temperature. The growth of zircon is common in eclogites during retrogression and post-collisional hydrothermal events (e.g., Sartini-Rideout et al., 2009; Zheng et al., 2007). Breakdown of clinopyroxene and garnet of the peak-*P* assemblage liberates Zr to the matrix and facilitates zircon growth during the retrogressive hydration (e.g., Kohn et al., 2015). Fluid activity during Salinic, Acadian, and any following overprinting events (Hames et al., 1991; Robinson et al., 1998) might be responsible for the extensive retrogression in the region as well as the rarity of HP terranes in the Taconic orogen. It is extremely unlikely, however, that this activity altered the U–Pb systematics in the interiors of pre-existing zircons (e.g., Breeding et al., 2004; Vorhies et al., 2013).

## 8. Geologic implications and conclusions

Stratigraphic analysis (Bradley, 1989) and regional tectonic reconstruction (Waldron et al., 2014) suggest that the Taconic Seaway was zipped southward. Our new metamorphic age adds to the preceding studies on Ordovician metamorphism from southern New England to Newfoundland, and helps to provide a geochronological test for this argument. Metamorphic ages are summarized in Table A.5 and Fig. 14. We use the weighted average so that the precisions of the ages are accounted for. The Taconian metamorphic and deformation ages systematically decrease southward. The weighted average ages are 464.9 ± 3.3 Ma in Newfoundland, 461.9 ± 2.8 Ma in northern Vermont/southern Québec, and 455.5 ± 6 Ma in southern New England and southeastern New York. The 455.5 ± 6 Ma age in the southern section of the Taconic orogen is 9.4 ± 6.8 Myr younger than in Newfoundland, and a Student's t-test indicates that the means are statistically different at the 98.8% confidence level (two-tailed test). The reported ages do not necessarily correspond to the same event(s), but the statistics of the ages demonstrate differences in timing along strike.

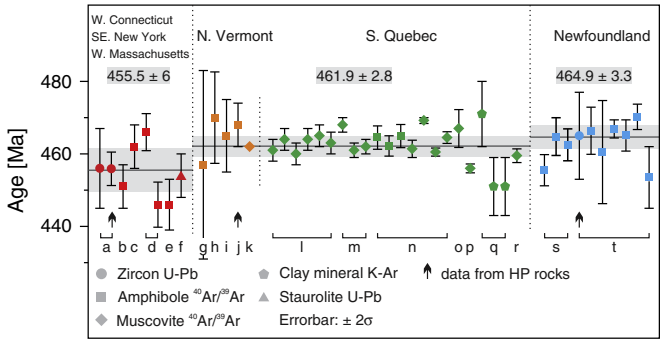


**Fig. 14.** Summary of reported Taconian metamorphic ages in the northern Appalachians from southeastern New York to Newfoundland (tabulated in Table A.5). The data from high pressure rocks are indicated by arrows. Error bars represent ± 2σ uncertainties. The weighted average ages are presented for the regions (band width ± 2σ).
Data sources: a. this study; b. Dallmeyer (1975) (plateau age recalculated in this study, Fig. A.9); c. Dallmeyer and Sutter (1976) (plateau age recalculated in this study, Fig. A.9); d. Sutter et al. (1985); e. Hames et al. (1991); f. Lanzirotti and Hanson (1997); g. Lanphere and Albee (1974); h. Laird et al. (1984); i. Laird et al. (1984), revised in Laird et al. (1993); j. Laird et al. (1993); k. Hames and Hodges (1993); l. Whitehead et al. (1996); m. Castonguay et al. (1997); n. Castonguay et al. (2001); o. Schroetter et al. (2006); p. Castonguay et al. (2007); q. Sasseville et al. (2008); r. De Souza et al. (2014); s. Dallmeyer and Williams (1975) (plateau age recalculated in this study, Fig. A.9); t. Castonguay et al. (2014).

Based on a comprehensive compilation of petro-tectonic data in the Taconic orogen, van Staal et al. (1998) proposed that the subduction polarity reversal also likely progressed diachronously southward, following the oblique continent–arc collision. In Newfoundland, the coeval metamorphism (ca. 467 Ma) and syn-collisional magmatism (ca. 470–460 Ma) provide an important time constraint for the break-off of the east-dipping subducting slab and the subduction polarity reversal (Castonguay et al., 2014; van Staal et al., 2007).

In northwest Connecticut, our new age results document high-pressure metamorphism at about 456 Ma, when the Laurentian margin collided with the Taconic arc. The *P–T* path involves post-peak-*T* compression (Fig. 9), typical for a "hard" collision process — when the Laurentian continent entered the subduction channel, the lateral compression caused intense deformation and thickening in the collision zone (Pehrsson et al., 2003; van Staal et al., 2007). The onset of subduction of the Laurentian margin is also reflected by the increasing continental components in the Taconian–Grampian arc magmatism (e.g., Draut and Clift, 2001; Ryan and Dewey, 2011). The zircon cores of Grenvillian age confirm the Laurentian affinity of the rocks, so that the recorded Ordovician events correspond to the east-dipping subduction of Laurentia beneath the overriding arc.

The Taconic collision was largely complete by 454 ± 2 Ma — the oldest age of the Brookfield plutonic series in western Connecticut (Sevigny and Hanson, 1995). This series cuts the Taconian lithologic lineation and fold structures and, thus, postdates earlier Taconian deformation and subduction polarity reversal. The 456–454 Ma bracket coincides with the termination of arc and/or collision related magmatism over the east-dipping subduction zone; the magmatism hiatus (460–456 Ma) between the Ammonoosuc sequence and the overling Quimby sequence is interpreted to correspond to the switched subduction polarity (Moench and Aleinikoff, 2003). The HP metamorphism (456 Ma), volcanic hiatus (460–456 Ma), and the 454 Ma stitching plutons provide a tight time constraint on the subduction polarity reversal in southern New England.

In sum, mafic gneiss in northwest Connecticut underwent high-pressure eclogite facies metamorphism (>14 kbar at ~700 °C). The protoliths were likely Early Cambrian rifting-related dikes. They reached peak pressure conditions when the "hard" collision took place between the Laurentian margin and the Taconic arc or arcs at ~456 Ma over an east-dipping subduction/collision zone. After the culmination of collision the subduction polarity switched. The collision was likely diachronous along strike — the HP metamorphism and subduction polarity reversal took place about 10 Myr later in Connecticut than in Newfoundland. We suggest that rocks with HP histories may be more common than recognized in New England, but that such histories were largely obscured by overprinting during exhumation or later orogenic activity.

## Acknowledgments

We thank O. Beyssac, M.T. Brandon, D.A.D. Evans, J.A. Gilotti, B.R. Hacker, J.H. Marsh, C. Merguerian, Y.Y. Podladchikov, D. Rumble III, A. Vitale Brovarone and C. Wei for thoughtful discussions, and D.M. Rye for careful editing. We appreciate the constructive reviews of F.S. Spear and an anonymous referee, as well as the reviews of C.R. van

Staal and two anonymous referees on an earlier version. Connecticut State Geologist M.A. Thomas kindly granted the access to the exposures in the Dennis Hill Mountain State Park. We gratefully acknowledge J.O. Eckert, Jr. for help with the electron microprobe at Yale University; A.K. Schmitt and R.C. Economos for help with SIMS zircon U–Pb dating at UCLA; and support from Yale University.

## Appendix A. Supplementary data

Supplementary data to this article can be found online at http://dx.doi.org/10.1016/j.lithos.2015.10.011.

## References

Ague, J.J., 1994. Mass transfer during Barrovian metamorphism of pelites, south-central Connecticut: I. Evidence for changes in composition and volume. American Journal of Science 294, 989–1057.
Ague, J.J., 1998. Simple models of coupled fluid infiltration and redox reactions in the crust. Contributions to Mineralogy and Petrology 132, 180–197.
Ague, J.J., Baxter, E.F., 2007. Brief thermal pulses during mountain building recorded by Sr diffusion in apatite and multicomponent diffusion in garnet. Earth and Planetary Science Letters 261, 500–516.
Ague, J.J., Eckert Jr., J.O., 2012. Precipitation of rutile and ilmenite needles in garnet: implications for extreme metamorphic conditions in the Acadian Orogen, USA. American Mineralogist 97, 840–855.
Ague, J.J., Nicolescu, S., 2014. Carbon dioxide released from subduction zones by fluid-mediated reactions. Nature Geoscience 7, 355–360.
Ague, J.J., Eckert Jr., J.O., Chu, X., Baxter, E.F., Chamberlain, C.P., 2013. Discovery of ultrahigh-temperature metamorphism in the Acadian orogen, Connecticut, USA. Geology 41, 271–274.
Allen, J.S., Thomas, W.A., Lavoie, D., 2009. Stratigraphy and structure of the Laurentian rifted margin in the northern Appalachians: a low-angle detachment rift system. Geology 37, 335–338.
Anderson, E.D., Moecher, D.P., 2007. Omphacite breakdown reactions and relation to eclogite exhumation rates. Contributions to Mineralogy and Petrology 54, 253–277.
Antignano, A., Manning, C.E., 2008. Rutile solubility in $H_2O$, $H_2O$–$SiO_2$, and $H_2O$–$NaAlSi_3O_8$ fluids at 0.7–2.0 GPa and 700–1000 °C: implications for mobility of nominally insoluble elements. Chemical Geology 255, 283–293.
Ayers, J.C., Watson, E.B., 1991. Solubility of apatite, monazite, zircon, and rutile in supercritical aqueous fluids with implications for subduction zone geochemistry. Philosophical Transactions of the Royal Society A 355, 365–375.
Bernini, D., Audétat, A., Dolejš, D., Keppler, H., 2013. Zircon solubility in aqueous fluids at high temperatures and pressures. Geochimica et Cosmochimica Acta 119, 178–187.
Bradley, D.C., 1989. Taconic plate kinematics as revealed by foredeep stratigraphy, Appalachian orogen. Tectonics 8, 1037–1049.
Breeding, C.M., Ague, J.J., Grove, M., Rupke, A.L., 2004. Isotopic and chemical alteration of zircon by metamorphic fluids; U–Pb age depth-profiling of zircon crystals from Barrow's garnet zone, northeast Scotland. American Mineralogist 89, 1067–1077.
Burton, W.C., Southworth, S., 2010. A model for Iapetan rifting of Laurentia based on Neoproterozoic dikes and related rocks. Geological Society of America Memoirs 206, 455–476.
Carswell, D.A., Tucker, R.D., O'Brien, P.J., Krogh, T.E., 2003. Coesite micro-inclusions and the U/Pb age of zircons from the Hareidland Eclogite in the Western Gneiss Region of Norway. Lithos 67, 181–190.
Castonguay, S., Tremblay, A., Ruffet, G., Féraud, G., Pinet, N., Sosson, M., 1997. Ordovician and Silurian metamorphic cooling ages along the Laurentian margin of the Québec Appalachians: bridging the gap between New England and Newfoundland. Geology 25, 583–586.
Castonguay, S., Ruffet, G., Tremblay, A., Féraud, G., 2001. Tectonometamorphic evolution of the southern Québec Appalachians: $^{40}Ar/^{39}Ar$ evidence for Middle Ordovician crustal thickening and Silurian–Early Devonian exhumation of the internal Humber zone. Geological Society of America Bulletin 113, 144–160.
Castonguay, S., Ruffet, G., Tremblay, A., 2007. Dating polyphase deformation across low-grade metamorphic belts: an example based on $^{40}Ar/^{39}AR$ muscovite age constraints from the southern Québec Appalachians, Canada. Geological Society of America Bulletin 119, 978–992.
Castonguay, S., Kim, J., Thompson, P.J., Gale, M.H., Joyce, N., Laird, J., Doolan, B.L., 2012. Timing of tectonometamorphism across the Green Mountain anticlinorium, northern Vermont Appalachians: $^{40}Ar/^{39}Ar$ data and correlations with southern Québec. Geological Society of America Bulletin 124, 352–367.
Castonguay, S., van Staal, C.R., Joyce, N., Skulski, T., Hibbard, J.P., 2014. Taconic metamorphism preserved in the Bale Verte Peninsular, Newfoundland Appalachians: geochronological evidence for ophiolite obduction and subduction and exhumation of the leading edge of the Laurentian (Humber) margin during closure of the Taconic Seaway. Geoscience Canada 41, 459–483.
Cawood, P.A., Dunning, G.R., Lux, D., van Gool, J.A.M., 1994. Timing of peak metamorphism and deformation along the Appalachian margin of Laurentia in Newfoundland: Silurian, not Ordovician. Geology 22, 399–402.
Chu, X., Ague, J.J., 2013. Phase equilibria for graphitic metapelite including solution of $CO_2$ in melt and cordierite: implications for dehydration, partial melting and graphite precipitation. Journal of Metamorphic Geology 31, 843–862.
Chu, X., Ague, J.J., 2015. Analysis of experimental data on divalent cation diffusion kinetics in aluminosilicate garnets with application to timescales of peak Barrovian metamorphism, Scotland. Contributions to Mineralogy and Petrology 170, 1–27.
Coggon, R., Holland, T.J.B., 2002. Mixing properties of phengitic micas and revised garnet–phengite thermobarometers. Journal of Metamorphic Geology 20, 683–696.
Dallmeyer, R.D., 1975. Release spectra of biotite and hornblende from the Cortlandt and Rosetown plutons, New York, and their regional implications. The Journal of Geology 5, 629–643.
Dallmeyer, R.D., Sutter, J.F., 1976. $^{40}Ar/^{39}Ar$ incremental-release ages of biotite and hornblende from variably retrograded basement gneisses of the northeasternmost Reading Prong, New York: their bearing on early Paleozoic metamorphic history. American Journal of Science 276, 731–747.
Dallmeyer, R.D., Williams, H., 1975. $^{40}Ar/^{39}Ar$ ages from the Bay of Islands Metamorphic Aureole: their bearing on the timing of Ordovician ophiolite obduction. Canadian Journal of Earth Sciences 12, 1685–1690.
Dannis, A.J., Shervais, J.W., Secor, D.T., 2000. Newberry, South Carolina eclogite. Structural setting and style of occurrences. In: Abate, A., Maybin, A.B. (Eds.), A Compendium of Field Trips of South Carolina Geology. South Carolina Geological Survey, pp. 29–39.
De Souza, S., Tremblay, A., 2015. A newly identified Gondwanan terrane in the Northern Appalachian Mountains: implication for the Taconic orogeny and the closure of the Iapetus Ocean: comment. Geology 43, e356.
De Souza, S., Tremblay, A., Ruffet, G., 2014. Taconian orogenesis, sedimentation and magmatism in the southern Québec-northern Vermont Appalachians: stratigraphic and detrital mineral record of Iapetan suturing. American Journal of Science 314, 1065–1103.
De Wit, M.J., Strong, D.F., 1975. Eclogite-bearing amphibolites from the Appalachian mobile belt, northwest Newfoundland: dry versus wet metamorphism. Journal of Geology 83, 609–627.
Diener, J.F.A., Powell, R., White, R.W., Holland, T.J.B., 2007. A new thermodynamic model for clino- and orthoamphiboles in the system $Na_2O$–$CaO$–$FeO$–$MgO$–$Al_2O_3$–$SiO_2$–$H_2O$–$O$. Journal of Metamorphic Geology 25, 631–656.
Draut, A.E., Clift, P.D., 2001. Geochemical evolution of arc magmatism during arc–continent collision, South Mayo, Ireland. Geology 29, 543–546.
Ellis, D.J., Thompson, A.B., 1986. Subsolidus and partial melting reactions in the quartz excess $CaO + MgO + Al_2O_3 + SiO_2 + H_2O$ system under water-excess and water-deficient conditions to 10 kbar: some implications for the origin of peraluminous melts from mafic rocks. Journal of Petrology 27, 91–121.
Eskola, P., 1921. On the eclogite of Norway. Skrifter Utgitt av det Norske VidenskapsselskChristiana, Matematisk-Naturvidenskapelig Klasse 18 pp. 1–118.
Evans, T.P., 2004. A method for calculating effective bulk composition modification due to crystal fractionation in garnet-bearing schist: implications for isopleth thermobarometry. Journal of Metamorphic Geology 22, 547–557.
Franceschelli, M., Puxeddu, M., Cruciani, G., Utzeri, D., 2007. Metabasites with eclogite facies relics from Variscides in Sardinia, Italy: a review. International Journal of Earth Sciences 96, 795–815.
Franz, G., Thomas, S., Smith, D.C., 1986. High-pressure phengite decomposition in Weissenstein eclogite, Münchberger Gneiss Massif, Germany. Contributions to Mineralogy and Petrology 92, 71–85.
Gao, J., John, T., Klemd, R., Xiong, X., 2007. Mobilization of Ti–Nb–Ta during subduction: evidence from rutile bearing dehydration segregations and veins hosted in eclogite, Tianshan, NW China. Geochimica et Cosmochimica Acta 71, 4974–4996.
Gates, R.M., 1975. The bedrock geology of the South Canaan quadrangle. Connecticut Geological and Natural History Survey Quadrangle Report 32 (33 pp.).
Ghiorso, M.S., Evans, B.W., 2008. Thermodynamics of rhombohedral oxide solid solutions and a revision of the Fe–Ti two-oxide geothermometer and oxygen-barometer. American Journal of Science 208, 957–1039.
Gilotti, J.A., Nutman, A.P., Brueckner, H.K., 2004. Devonian to Carboniferous collision in the Greenland Caledonides: U–Pb zircon and Sm–Nd ages of high-pressure and ultrahigh-pressure metamorphism. Contributions to Mineralogy and Petrology 148, 216–235.
Green, E., Holland, T.J.B., Powell, R., 2007. An order–disorder model for omphacitic pyroxenes in the system jadeite–diopside–hedenbergite–acmite, with applications to eclogitic rocks. Journal of Metamorphic Geology 92, 1181–1189.
Groppo, C., Rolfo, F., Liu, Y.-C., Deng, L.-P., Wang, A.-D., 2015. P–T evolution of elusive UHP eclogites from the Luotian dome (North Dabie Zone, China): how far can the thermodynamic modeling lead us? Lithos 226, 183–200.
Hames, W.E., Hodges, K.V., 1993. Laser $^{40}Ar/^{39}Ar$ evaluation of slow cooling and episodic loss of $^{40}Ar$ from a sample of polymetamorphic muscovite. Science 261, 1721–1723.
Hames, W.E., Tracy, R.J., Ratcliffe, N.M., Sutter, J.F., 1991. Petrologic, structural, and geochronologic characteristics of the Acadian metamorphic overprint on the Taconide Zone in part of southwestern New England. American Journal of Science 291, 887–913.
Hames, W.E., Hogen, J.P., Gilbert, M.C., 1998. Revised granite–gabbro age relationships, southern Oklahoma Aulacogen USA. Basement Tectonics 12 pp. 247–249.
Harrison, T.M., 1982. Diffusion of $^{40}Ar$ in hornblende. Contributions to Mineralogy and Petrology 78, 324–331.
Harwood, D.S., 1975. Fold thrust tectonism in the southern Berkshire massif, Connecticut and Massachusetts. In: Ratcliffe, N.M. (Ed.), Guidebook to Field Trips in Western Mass., Northern Conn. and Adjacent Areas of New York. NEIGC, City College, New York, pp. 122–143.
Harwood, D.S., 1979a. Geologic map of the Norfolk quadrangle, Connecticut. USGS Geologic Quadrangle Maps 1518, scale 1:24 000, 1 sheet.
Harwood, D.S., 1979b. Geologic map of the South Sandisfield Quadrangle, Massachusetts and Connecticut. USGS Geologic Quadrangle Maps 1519, scale 1:24 000, 1 sheet.
Holland, T.J.B., Powell, R., 1998. An internally-consistent thermodynamic dataset for phases of petrological interest. Journal of Metamorphic Geology 16, 309–344.

Holland, T., Powell, R., 2003. Activity–composition relations for phases in petrological calculations: an asymmetric multicomponent formulation. Contributions to Mineralogy and Petrology 145, 492–501.
Hollister, L.S., 1966. Garnet zoning: an interpretation based on the Rayleigh fractionation model. Science 154, 1647–1651.
Jamieson, R.A., 1990. Metamorphism of an Early Paleozoic continental margin, western Baie Verte Peninsula, Newfoundland. Journal of Metamorphic Geology 8, 269–288.
Janak, M., Ravna, E.J.K., Kullerud, K., 2012. Constraining peak *P–T* conditions in UHP eclogites: calculated phase equilibria in kyanite- and phengite-bearing eclogite of the Tromsø Nappe, Norway. Journal of Metamorphic Geology 30, 377–396.
Karabinos, P.A., Aleinikoff, J.N., 1990. Evidence for a major Proterozoic, post-Grenvillian igneous event in western New England. American Journal of Science 290, 959–974.
Karabinos, P.A., Samson, S.D., Hepburn, J.C., Stoll, H.M., 1998. Taconian orogeny in the New England Appalachians: collision between Laurentia and the Shelburne Falls arc. Geology 26, 215–218.
Kohn, M.J., Spear, F., 2000. Retrograde net transfer reaction insurance for pressure–temperature estimate. Geology 12, 1127–1130.
Kohn, M.J., Corrie, S.L., Markley, C., 2015. The fall and rise o metamorphic zircon. American Mineralogist 100, 897–908.
Konrad-Schmolke, M., O'Brien, P.J., Zack, T., 2011. Fluid migration above a subducted slab—constraints on amount, pathways and major element mobility from partially overprinted eclogite-facies rocks (Sesia Zone, Western Alps). Journal of Petrology 52, 457–486.
Laird, J., 1988. Arenig to Wenlock age metamorphism in the Appalachians. In: Harris, A.L., Fettes, D.J. (Eds.), The Caledonian–Appalachian OrogenGeological Society Special Publication 38, 311–345.
Laird, J., Albee, A.L., 1981. Pressure, temperature, and time indicators in mafic schist; their application to reconstructing the polymetamorphic history of Vermont. American Journal of Science 281, 97–126.
Laird, J., Lanphere, M.A., Albee, A.L., 1984. Distribution of Ordovician and Devonian metamorphism in mafic and pelitic schists from northern Vermont. American Journal of Science 284, 376–413.
Laird, J., Trzcienski, W.E., Bothner, W.A., 1993. High-pressure Taconian and subsequent polymetamorphism of southern Québec and northern Vermont. In: Cheney, J.T., Hepburn, J.C. (Eds.), Field Trip Guidebook for the Northeastern United States: 1993 Boston, GSA vol. 2. Geological Society of America, Boulder, Colorado, pp. 1–32.
Lambert, D.D., Unruh, D.M., Gilbert, M.C., 1988. Rb–Sr and Sm–Nd isotopic study of the Glen Mountains layered complex: initiation of rifting within the southern Oklahoma aulacogen. Geology 16, 13–17.
Lang, H.M., Gilotti, J.A., 2015. Modeling the exhumation path of partially melted ultrahigh-pressure metapelities, North-East Greenland Caledonides. Lithos 226, 131–146.
Lanphere, M.A., Albee, A.L., 1974. $^{40}Ar/^{39}Ar$ age measurements in the Worcester Mountains: evidence of Ordovician and Devonian metamorphic events in Northern Vermont. American Journal of Science 274, 545–555.
Lanzirotti, A., Hanson, G.N., 1997. An assessment of the utility of staurolite in U–Pb dating of metamorphism. Contributions to Mineralogy and Petrology 129, 352–365.
Lavoie, D., Burden, E., Lebel, D., 2003. Stratigraphic framework for the Cambrian Ordovician rift and passive margin successions from southern Québec to western Newfoundland. Canadian Journal of Earth Sciences 40, 177–205.
Leake, B.E., Woolee, A.R., Arps, C.E.S., et al., 1997. Nomenclature of amphiboles: report of the subcommittee on amphiboles of the International Mineralogical Association, commission on new minerals and mineral names. American Mineralogist 82, 1019–1037.
Lin, S., Brem, A.G., van Staal, C.R., Davis, D.W., McNicoll, V.J., Pehrsson, S., 2013. The Corner Brook Lake block in the Newfoundland Appalachians: a suspect terrane along the Laurentian margin and evidence for large-scale orogen-parallel motion. Geological Society of America Bulletin 125, 1618–1632.
Ludwig, K.R., 2008. User's Manual for Isoplot 3.70, a Geochronological Toolkit for Microsoft Excel: Berkeley Geochronological Center, Special Publication No. 4. pp. 1–76.
Luvizotto, G.L., Zack, T., 2009. Nb and Zr behavior in rutile during high-grade metamorphism and retrogression: an example from the Ivrea–Verbano Zone. Chemical Geology 261, 303–317.
Macdonald, F.A., Ryan-Davis, J., Coish, R.A., Crowley, J.L., Karabinos, P., 2014. A newly identified Gondwanan terrane in the northern Appalachian Mountains: implications for the Taconic orogeny and closure of the Iapetus Ocean. Geology 42, 539–542.
Maggs, W.W., 1984. Garnet + Clinopyroxene–Plagioclase Symplectite Lenses in the Berkshire Massif (B.A. Thesis) Amherst College, Northwest Connecticut.
Maggs, W.W., Spear, F.S., Cheney, J.T., 1986. Probable retrograded eclogites in the Berkshire Massif. GSA Northeast Section Meeting, Abstracts with Programs 18 p. 32.
Manning, C.E., 2004. The chemistry of subduction-zone fluid. Earth and Planetary Science Letters 223, 1–16.
Meschede, M., 1986. A method of discriminating between different types of mid-ocean ridge basalts and continental tholeiites with the Nb–Zr–Y diagram. Chemical Geology 78, 558–569.
Mihok-Trenka, C., 2004. Taconian Omphacite-bearing Assemblages in the Manhattan Prong (Master Thesis) Queens College of C.U.N.Y., Southeast New York (92 pp.).
Moench, R.H., Aleinikoff, J.N., 2003. Stratigraphy, geochronology, and accretionary terrane settings of two Bronson Hill arc sequences, northern New England. Physics and Chemistry of the Earth 28, 113–160.
Nahodilová, R., Faryad, S.W., Dolejš, D., Tropper, P., Konzett, J., 2011. High-pressure partial melting and melt loss in felsic granulites in the Kutná Hora complex, Bohemian Massif (Czech Republic). Lithos 125, 641–658.
Nakano, N., Osanai, Y., Sajeev, K., Hayasaka, Y., Miyamoto, T., Minh, N.T., Owada, M., Windley, B., 2010. Triassic eclogite from northern Vietnam: inferences and geological significance. Journal of Metamorphic Geology 28, 59–76.
Osberg, P.H., 1969. Lower Paleozoic stratigraphy and structural geology, Green Mountain–Sutton Mountain Anticlinorium, Vermont and southern Quebec. In: Kay, G.M. (Ed.), North Atlantic—Geology and Continental Drift. A Symposium on the Origin of the Atlantic OceanAmerican Association of Petroleum Geologists Memoir 12, 687–700.
Page, F.Z., Essene, E.J., Mukasa, S.B., 2003. Prograde and retrograde history of eclogites from the Eastern Blue Ridge, North Carolina, USA. Journal of Metamorphic Geology 21, 685–698.
Page, F.Z., Essen, E.J., Mukasa, S.B., 2005. Quartz exsolution in clinopyroxene is not proof of ultrahigh pressures: evidence from eclogites from the Eastern Blue Ridge, Southern Appalachians USA. American Mineralogist 90, 1092–1099.
Pearce, J.A., 1982. Trace element characteristics of lavas from eruptive setting of lavas from destructive plate boundaries. In: Thorpe, R.S. (Ed.), Andesites. Wiley, Chichester, pp. 525–548.
Pearce, J.A., Cann, J.R., 1973. Tectonic setting of basic volcanic rocks determined using trace element analyses. Earth and Planetary Science Letters 19, 290–300.
Pehrsson, S., van Staal, C.R., Herd, R.K., McNicoll, V., 2003. The Cornacks Lake Complex, Dashwoods Subzone: a window into the deeper levels of the Notre Dame Arc. In: Pereira, C.P.C., Walsh, D.G., Kean, B.F. (Eds.), Current Research 2002. Newfoundland Department of Mines and Energy, Geological Survey, Report 2002-1, pp. 115–125.
Powell, R., Holland, T.J.B., Worley, B., 1998. Calculating phase diagrams involving solid solutions via non-linear equations, with examples using THERMOCALC. Journal of Metamorphic Geology 16, 577–588.
Rapp, J.F., Klemme, S., Butler, I.B., Harley, S.L., 2010. Extremely high solubility of rutile in chloride and fluoride-bearing metamorphic fluids: an experimental investigation. Geology 38, 323–326.
Ratcliffe, N.M., Hames, W.E., Stanley, R.S., 1998. Interpretation of ages of arc magmatism, metamorphism, and collisional tectonics in the Taconian Orogen of western New England. American Journal of Science 298, 791–797.
Rivers, T., 1997. Lithotectonic elements of the Grenville Province: review and tectonic implications. Precambrian Research 86, 117–154.
Robinson, P., Tucker, R.D., Bradley, D., Henry IV, N.B., Osberg, P.H., 1998. Paleozoic orogens in New England, USA. Geologiska Föreningens i Stockholm Förhandlingar 120, 119–148.
Rollinson, H.R., 1993. Using geochemical data: evaluation, presentation and interpretation. Longman Geochemistry Series. Longman, Harlow, UK (325 pp.).
Ryan, P.D., Dewey, J.F., 2011. Arc–continent collision in the Ordovician of western Ireland: stratigraphic, structural and metamorphic evolution. In: Brown, D., Ryan, P.D. (Eds.), Arc Continent Collision. Springer, Berlin, pp. 373–401.
Sartini-Rideout, C., Gilotti, J.A., McClelland, W.C., 2009. Reaction progress and timing of retrogression of eclogite-facies rocks, Danmarkshavn, North-East Greenland Caledonides. European Journal of Mineralogy 21, 1149–1172.
Sasseville, C., Tremblay, A., Clauer, N., Liewig, N., 2008. K–Ar age constraints on the evolution of polydeformed fold–thrust belts: the case of the Northern Appalachians (southern Québec). Journal of Geodynamics 45, 99–119.
Schmädicke, E., Okrusch, M., Schmidt, W., 1992. Eclogite-facies rocks in the Saxonian Erzgebirge, Germany: high pressure metamorphism under contrasting P–T conditions. Contributions to Mineralogy and Petrology 110, 226–241.
Schmalholz, S.M., Podladchikov, Y.Y., 2013. Tectonic overpressure in weak crustal-scale shear zones and implications for the exhumation of high-pressure rocks. Geophysical Research Letters 40, 1984–1988.
Schmidt, M.W., Poli, S., 2004. Magmatic epidote. Reviews in Mineralogy and Geochemistry 56, 399–430.
Schmitz, M.D., Bowring, S.A., Ireland, T.R., 2003. Evaluation of Duluth Complex anorthosite series (AS3) zircon as a U–Pb geochronological standard: new high-precision isotope dilution thermal ionization mass spectrometry results. Geochimica et Cosmochimica Acta 67, 3665–3672.
Schroetter, J.M., Tremblay, A., Bedard, J.H., Villeneuve, M., 2006. Syncollisional basin development in the Appalachian orogen: the Saint Daniel mélange, southern Québec, Canada. Geological Society of America Bulletin 118, 109–125.
Sevigny, J.H., Hanson, G.N., 1995. Late-Taconian and pre-Acadian history of the New England Appalachians of southwestern Connecticut. Geological Society of America Bulletin 107, 487–498.
Shervais, J.W., Dennis, A.J., McGee, J.J., Secor, D., 2003. Deep in the heart of Dixie: pre-Alleghanian eclogite and HP granulite metamorphism in the Carolina Terrane, South Carolina, USA. Journal of Metamorphic Geology 21, 65–80.
Spear, F.S., 1988. Metamorphic fractional crystallization and internal metasomatism by diffusional homogenization of zoned garnets. Contributions to Mineralogy and Petrology 99, 507–517.
Spear, F., 2014. The duration of near-peak metamorphism from diffusion modelling of garnet zoing. Journal of Metamorphic Geology 32, 903–914.
Spray, J.G., 1988. Retrograde eclogite from Mont Albert, Gaspé, Quebec: discussion. Canadian Journal of Earth Sciences 25, 1542–1543.
Stanley, R.S., Ratcliffe, N.M., 1985. Tectonic synthesis of the Taconian orogeny in western New England. Geological Society of America Bulletin 96, 1227–1250.
Štípská, P., Powell, R., Racek, M., 2014. Rare eclogite–mafic granulite in felsic granulite in Blanský les: precursor of intermediate granulite in the Bohemian Massif. Journal of Metamorphic Geology 32, 325–345.
Sun, S.S., McDonough, W.F., 1989. Chemical and isotopic systematics of oceanic basalts: implications for mantle composition and processes. In: Saunders, A.D., Morry, M.J. (Eds.), Magmatism in the Ocean BasinsGeological Society of London, Special Publication 42, 313–345.
Sutter, J.F., Ratcliffe, N.M., Mukasa, S.B., 1985. $^{40}Ar/^{39}Ar$ and K–Ar data bearing on the metamorphic and tectonic history of western New England. Geological Society of America Bulletin 96, 123–146.
Tomkins, H.S., Powell, R., Ellis, D.J., 2007. The pressure dependence of the zirconium-in-rutile thermometer. Journal of Metamorphic Geology 25, 703–713.

Trzcienski Jr., W.E., 1988. Retrograde eclogite from Mont Albert, Gaspé, Quebec. Canadian Journal of Earth Sciences 25, 30–37.
van Staal, C.R., Barr, S.M., 2012. Lithospheric architecture and tectonic evolution of the Canadian Appalachians and associated Atlantic margin. Chapter 2. In: Percival, J.A., Cook, F.A., Clowes, R.M. (Eds.), Tectonic Styles in Canada: The LITHOPROVE Perspective. Geological Association of Canada, Special Paper 49, 41–95.
van Staal, C.R., Dewey, J.F., Mac Niocaill, C., McKerrow, W.S., 1998. The Cambrian–Silurian tectonic evolution of the northern Appalachians and British Caledonides: history of a complex, west and southwest Pacific-type segment of Iapetus. Geological Society of London, Special Publication 143, 199–242.
van Staal, C.R., Whalen, J.B., McNicoll, V.J., Persson, S., Lissenberg, C.J., Zagorevski, A., van Breemen, O., Jenner, G.A., 2007. The Notre Dame arc and the Taconic orogeny in Newfoundland. Geological Society of America Memoirs 200, 511–552.
van Staal, C.R., Barr, S.M., Murphy, J.B., 2012. A paleogeographical review of the peri-Gondwanan realm of the Appalachian orogeny. Geology 11, 987–990.
Vogel, D.E., 1966. Nature and chemistry of the formation of clinopyroxene–plagioclase symplectite form omphacite. Neues Jahrbuch für Mineralogie 6, 185–189.
Vorhies, S.H., Ague, J.J., Schmitt, A.K., 2013. Zircon growth and recrystallization during progressive metamorphism, Barrovian zones, Scotland. American Mineralogist 98, 219–230.
Waldron, J.W.F., Schofield, D.I., Murphy, J.B., Thomas, C.W., 2014. How was the Iapetus Ocean infected with subduction? Geology 42, 1095–1098.
Watson, E.B., Wark, D.A., Thomas, J.B., 2006. Crystallization thermometers for zircon and rutile. Contributions to Mineralogy and Petrology 151, 413–433.
White, C.E., Barr, S.M., Jamieson, R.A., Reynolds, P.H., 2001. Neoproterozoic high-pressure/low-temperature metamorphic rocks in the Avalon terrane, southern New Brunswick, Canada. Journal of Metamorphic Geology 19, 519–530.
White, R.W., Powell, R., Clarke, G.L., 2002. The interpretation of reaction textures in Ferich metapelitic granulites of the Musgrave Block, central Australia: constraints from mineral equilibria calculations in the system $K_2O$–FeO–MgO–$Al_2O_3$–$SiO_2$–$H_2O$–$TiO_2$–$Fe_2O_3$. Journal of Metamorphic Geology 20, 41–55.
White, R.W., Powell, R., Holland, T.J.B., 2007. Progress relating to calculation of partial melting equilibria for metapelites. Journal of Metamorphic Geology 25, 511–527.
Whitehead, J., Heynolds, P.H., Spray, J.G., 1996. $^{40}Ar/^{39}Ar$ age constraints on Taconian and Acadian events in the Québec Appalachians. Geology 24, 359–362.
Wiedenbeck, M., Hanchar, J.M., Peck, M.H., et al., 2004. Further characterization of the 91500 zircon crystal. Geostandards and Geoanalytical Research 28, 9–39.
Will, T.M., Schmädicke, E., 2001. A fist find of retrogressed eclogites in the Odenwald Crystalline Complex, Mid-German crystalline Rise, Germany: evidence for a so far unrecognized high pressure metamorphism in the Central Variscides. Lithos 59, 109–125.
Willard, R.A., Adams, M.G., 1994. Newly discovered eclogite in the southern Appalachian orogen, northwestern North Carolina. Earth and Planetary Science Letters 123, 61–70.
Wood, D.A., 1980. The application of a Th–Hf–Ta diagram to problems of tectonomagmatic classification and to establishing the nature of crustal contamination of basaltic lavas of the British Tertiary volcanic province. Earth and Planetary Science Letters 50, 11–30.
Zack, T., Moraes, R., Kronz, A., 2004. Temperature dependence of Zr in rutile: empirical calibration of a rutile thermometer. Contributions to Mineralogy and Petrology 148, 471–488.
Zheng, Y.-F., Gao, T.-S., Wu, Y.-B., Gong, B., Liu, X.M., 2007. Fluid flow during exhumation of deeply subducted continental crust: zircon U–Pb age and O-isotope studies of a quartz vein within ultrahigh-pressure eclogite. Journal of Metamorphic Geology 25, 267–283.